

1 **Detecting climate signals using explainable AI with**
2 **single-forcing large ensembles**

3 **Zachary M. Labe¹ and Elizabeth A. Barnes¹**

4 ¹Department of Atmospheric Science, Colorado State University, Fort Collins, CO, USA

5 **Key Points:**

- 6 • Using explainable AI methods with artificial neural networks (ANN) reveals cli-
7 mate patterns in large ensemble simulations
- 8 • An ANN trained using a large ensemble simulation without time-evolving aerosols
9 makes more accurate predictions of real world data
- 10 • A metric is proposed for quantifying the uncertainty of an ANN visualization method
11 that extracts signals from different external forcings

Abstract

It remains difficult to disentangle the relative influences of aerosols and greenhouse gases on regional surface temperature trends in the context of global climate change. To address this issue, we use a new collection of initial-condition large ensembles from the Community Earth System Model version 1 that are prescribed with different combinations of industrial aerosol and greenhouse gas forcing. To compare the climate response to these external forcings, we adopt an artificial neural network (ANN) architecture from previous work that predicts the year by training on maps of near-surface temperature. We then utilize layer-wise relevance propagation (LRP) to visualize the regional temperature signals that are important for the ANN's prediction in each climate model experiment. To mask noise when extracting only the most robust climate patterns from LRP, we introduce a simple uncertainty metric that can be adopted to other explainable artificial intelligence (AI) problems. We find that the North Atlantic, Southern Ocean, and Southeast Asia are key regions of importance for the neural network to make its prediction, especially prior to the early-21st century. Notably, we also find that the ANN performs better on inputs of observational data after training on the large ensemble experiment with industrial aerosols held fixed to 1920 levels. This work illustrates the sensitivity of regional temperature signals to changes in aerosol forcing in historical simulations. By using explainable AI methods, we have the opportunity to improve our understanding of (non)linear combinations of anthropogenic forcings in state-of-the-art global climate models.

Plain Language Summary

Using a machine learning method called artificial neural networks, we explore how human-caused climate drivers can affect regional patterns of surface temperature. Here we use a climate model with different combinations of greenhouse gases and industrial aerosols (particles in the atmosphere) to understand their influence on climate change and variability. By employing visualization tools to see how the artificial neural network makes its predictions, we can better recognize how these climate drivers influence global temperature in the past, present, and future. For instance, we find that aerosols emitted in the 20th century and early 21st century have obstructed our view of global warming in some areas of the world, such as over the North Atlantic Ocean. Machine learn-

ing accompanied by new visualization methods have the potential to bring new insights
into understanding the effects of global climate change in observations and models.

1 Introductions

Separating human-induced climate forcing from internal variability remains a key challenge for attributing and communicating the impacts of global climate change on regional scales. While state-of-the-art global climate models (GCMs) include anthropogenic (e.g., greenhouse gases and aerosols) and natural (e.g., volcanoes) radiative forcings, it remains difficult to understand their combined interactions and associated effects on climate variability (Stocker et al., 2013). The chaotic noise of the atmosphere (internal variability) also gives rise to additional uncertainties on seasonal to multi-decadal timescales (Deser et al., 2012; Kay et al., 2015). For this reason, it still is difficult to constrain and reduce the uncertainty in Earth’s equilibrium climate sensitivity over the last several decades (Sherwood et al., 2020). Moreover, these complex interactions between internal and external climate forcings make it challenging to interpret the physical mechanisms driving regional and even global-scale temperature variability (Stott et al., 2006; Knutti et al., 2010; Maher et al., 2014; D. M. Smith et al., 2016; Medhaug et al., 2017; Hausteine et al., 2019; Mankin et al., 2020).

While greenhouse gas forcing dominates the overall climate change signal (net warming), an abundance of anthropogenic aerosols can also influence Earth’s surface temperature (net cooling) by scattering or absorbing incoming solar radiation (Bellouin et al., 2020). Further, recent studies have found an influence of anthropogenic aerosols on tropospheric temperatures (e.g., Santer et al., 2019; Mitchell et al., 2020), oceanic internal variability (e.g., Hausteine et al., 2019; Dagan et al., 2020; Meehl, Hu, et al., 2020; Qin et al., 2020), the hydrologic cycle (e.g., Marvel et al., 2019; Bonfils et al., 2020), and the large-scale atmospheric circulation (e.g., Allen & Sherwood, 2011; Wang et al., 2020). Meanwhile, less attention has been given to comparing regional climate trends to individual anthropogenic external forcings relative to the influence of internal variability (see examples by Polvani et al., 2011; Santer et al., 2019; Bonfils et al., 2020; Chemke et al., 2020; Deser, Phillips, et al., 2020). For instance, after using an initial-condition large ensemble, Oudar et al. (2018) found a larger role for internal variability than suggested by earlier Coupled Model Intercomparison Project Phase 5 (CMIP5) studies (e.g., D. M. Smith

74 et al., 2016) when attributing the impact of anthropogenic aerosols to the global mean
75 surface temperature trend in the early 21st century.

76 In addition to the influence of internal variability, the effective radiative forcing from
77 anthropogenic aerosol emissions also remains uncertain over the historical period (Booth
78 et al., 2018; Bellouin et al., 2020; Thorsen et al., 2020). In a novel experiment design,
79 Dittus et al. (2020) assessed the sensitivity of a climate model to a plausible range of his-
80 torical aerosol forcings. They found better agreement between the observed global mean
81 surface temperature record and an experiment with smaller net aerosol forcing than the
82 standard configuration of the GCM. Consequently, this suggests that temperature sig-
83 nals may be highly sensitive to small changes in aerosols, even when the aerosol forcing
84 in GCMs is constrained to fall within observational estimates (Dittus et al., 2020). This
85 also could be one explanation for the higher climate sensitivities found in CMIP6 mod-
86 els (Flynn & Mauritsen, 2020; Meehl, Senior, et al., 2020).

87 Recent advances in computational power have led to the development of a grow-
88 ing number of initial-condition large ensembles for assessing climate change and variabil-
89 ity (Deser, Lehner, et al., 2020; Deser, 2020). Within a single large ensemble GCM sim-
90 ulation, one can obtain the forced response (i.e., climate signal) by averaging across in-
91 dividual ensemble members that differ by only a small random perturbation error. Thus,
92 if the model is correct, observations of the real world should fall within the ensemble spread
93 in order to reflect both a common forced signal (climate change) and the unpredictable
94 noise of the atmosphere. In other words, the statistical characteristics of internal vari-
95 ability should be similar between the real world and the individual model ensemble mem-
96 bers. However, although numerous statistical methods have been proposed to further ex-
97 tract the forced response from internal variability (e.g., Hegerl et al., 1996; Deser et al.,
98 2016; Barnes et al., 2019; Santer et al., 2019; Sippel et al., 2019; Barnes et al., 2020; Sip-
99 ppel et al., 2020; Wills, Battisti, et al., 2020), the problem of climate pattern attribution
100 still remains difficult (Wills, Sippel, & Barnes, 2020).

101 To improve our understanding of the forced signals from individual anthropogenic
102 climate drivers amidst the noise of internal variability, we implement a method of ex-
103 plainable artificial intelligence (XAI) using data from a novel set of single-forcing large
104 ensemble experiments. The adoption of machine learning applications for geoscience is-
105 sues continues to rapidly grow (Ebert-Uphoff et al., 2019; McGovern et al., 2019; Rasu

106 et al., 2019; Boukabara et al., 2020; Toms et al., 2020; Watson-Parris, 2020), especially
107 due to an increasing number of XAI methods (Samek et al., 2017; Montavon et al., 2018;
108 Samek et al., 2020). Recently, machine learning models have been used for diverse ap-
109 plications in mesoscale meteorology (e.g., Gagne et al., 2019; Lagerquist et al., 2020),
110 numerical weather prediction (e.g., Rasp et al., 2020; Weyn et al., 2020), simulating cloud
111 and radiation processes in GCMs (e.g., Rasp et al., 2018), turbulence and convection pa-
112 rameterizations (e.g., Beucler et al., 2019; Zanna & Bolton, 2020), attribution of global
113 climate change (e.g., Barnes et al., 2019; Mansfield et al., 2020; Sippel et al., 2020), and
114 reconstructions of historical temperature trends (Kadow et al., 2020). To explore how
115 machine learning models are making their predictions, we focus on using XAI techniques
116 in order to gain new scientific insights for climate science.

117 In this study, we use artificial neural networks (ANN) in association with an ex-
118 plainability method called layer-wise relevance propagation (LRP) on data from climate
119 model simulations. By investigating the LRP results, we identify key climate pattern re-
120 sponses that are driven by distinct external forcings, namely, greenhouse gases and in-
121 dustrial aerosols. Finally, we assess the skill of the ANN by training on real world ob-
122 servations and introduce a metric to mask noise in assessing the LRP visualizations.

123 **2 Data and Methods**

124 **2.1 Climate Model Simulations**

125 For all climate model data, we use large ensemble simulations performed by the Com-
126 munity Earth System Model version 1 (CESM1; Hurrell et al., 2013) covering 1920 to
127 2080. CESM1 is a fully coupled GCM and is run with 30 vertical levels and a horizon-
128 tal resolution of 1° . The atmospheric model is the Community Atmosphere Model ver-
129 sion 5 (CAM5; Neale et al., 2012), which is coupled to interactive land, ocean, and sea
130 ice components.

131 Here, we first analyze the widely-used 40-member large ensemble as described in
132 Kay et al. (2015), which we refer to as “ALL” (for all-forcing). The large number of en-
133 semble members is useful for characterizing atmospheric internal variability (or noise)
134 in the climate system (Maher et al., 2019; Deser, Lehner, et al., 2020). Each of the en-
135 semble members have the same external forcing, but are generated from a small random
136 round-off difference in the atmospheric initial conditions. Historical forcing is imposed

137 from 1920 to 2005, and thereafter Representative Concentration Pathway 8.5 (RCP8.5;
138 Vuuren et al., 2011) is used to simulate a worst-case climate scenario through the end
139 of the 21st century (Peters & Hausfather, 2020). Land use/land cover changes, biomass
140 burning, and stratospheric ozone concentrations also evolve with time in the ALL sim-
141 ulation. Although large uncertainties exist, CESM1’s total aerosol effective radiative forc-
142 ing falls within one standard deviation of observational evidence (Zelinka et al., 2014;
143 Bellouin et al., 2020; Deser, Phillips, et al., 2020). We will return to this last point later
144 in the study.

145 In addition, we also use a set of two new single-forcing simulations from CESM1
146 that are both run with 20 ensemble members (Deser, Phillips, et al., 2020). These large
147 ensembles have the same GCM, initialization protocol, and external forcing as ALL, but
148 differ by one time-evolving forcing agent that is withheld per simulation. In particular,
149 greenhouse gas concentrations are held fixed to 1920 levels in one experiment (AER+),
150 and industrial aerosols are held fixed to 1920 levels in another (GHG+). While our no-
151 tation in this study reflects the dominant external forcing agent per simulation (either
152 greenhouse gases (GHG) or industrial aerosols (AER)), we do note that there are other
153 important climate feedbacks and natural variability included in each experiment (hence,
154 the “+” sign) that may contribute to our interpretation of the ANN results (e.g., Luys-
155 saert et al., 2014; Hawkins et al., 2017; Deng et al., 2020; Lehner et al., 2020; Maher et
156 al., 2020; Milinski et al., 2020). Since we only focus on one GCM (CESM1) with histor-
157 ical and RCP8.5 forcing, we can neglect the impact of any structural model and emis-
158 sions scenario uncertainties that would arise from using, for instance, CMIP5/6 (Hawkins
159 & Sutton, 2009; Knutti & Sedlacek, 2013; Lehner et al., 2020).

160 After taking into account the smaller ensemble size of the single-forcing runs, we
161 only consider the first 20 members of ALL. However, this does not affect the skill of the
162 ANN for training and testing data (not shown). We apply a bilinear interpolation to the
163 three sets of large ensembles so that they share a slightly coarser latitude by longitude
164 global grid ($1.9^\circ \times 2.5^\circ$). We only consider fields of monthly near-surface air tempera-
165 ture (TREFHT; °C) to calculate seasonal and annuals means from model output. An
166 overview of the climate model simulations used in this study can be found in Table S1.

2.2 Observations

To understand the effect of training on climate model simulations with different external forcing, we test the ANN on observations using the new National Oceanic and Atmospheric Administration/Cooperative Institute for Research in Environmental Sciences/Department of Energy (NOAA-CIRES-DOE) Twentieth Century Reanalysis (20CR) version 3 (20CRv3; also referred to here as ‘observations’) (Slivinski et al., 2019). Updates to 20CRv3 include an 80-member ensemble size for confidence estimation, a four-dimensional incremental analysis data assimilation scheme (4DIAU), and a higher resolution (T254) core model (described in Slivinski et al., 2019). These improvements lead to a reduction in biases of near-surface temperature, sea surface temperature, and sea level pressure compared to older versions of 20CR, especially in the early to mid-20th century (Compo et al., 2011; Giese et al., 2016). Further, 20CRv3 was found to be in close agreement with other independently derived reanalysis data sets, including the European Centre for Medium-Range Weather Forecasts (ECMWF) ERA-20C and CERA-20C (Slivinski et al., 2019, 2020).

We analyze monthly fields of 2-m air temperatures ($^{\circ}\text{C}$) from 20CRv3 after interpolating (bilinear) onto a common grid of 1.9° latitude by 2.5° longitude for consistency with the climate model simulations. 20CRv3 was selected for our analysis due to its temporally and spatially complete fields of 2-m temperature that are available globally from 1920 to 2015. Similar results were also obtained from the ANN after evaluating on the ECMWF ERA5 reanalysis (Hersbach et al., 2020) for the more recent 1979 to 2019 period. However, in this study, we focus our attention on 20CRv3 for consistency with the historical climate model output. A summary of the observations can be found in Table S2.

2.3 Neural Network Framework

In this analysis, we adopt a neural network architecture that was first introduced in Barnes et al. (2020) and is further illustrated here in Figure 1. We compare the impact of time-evolving greenhouse gases and industrial aerosols on a classification task of predicting the decade (year) from input maps of temperature. Each unit of the ANN input layer represents one grid point from a 2-m temperature map (13824 units per map with dimensions of 96 latitudes by 144 longitudes), and our output layer represents the

198 probabilities of a particular decade class (e.g., 2000-2009). For the time being, the cur-
199 rent method of ANN interpretation we use here (layer-wise relevance propagation; LRP)
200 has only been optimized for neural networks with classification algorithms (Bach et al.,
201 2015; Toms et al., 2020). Since we are interested in how the ANN determines its out-
202 put (i.e., looking into the black box), rather than the output itself, we frame our prob-
203 lem as a classification task for use of LRP.

204 Our ANN is set up with two hidden layers that each contain 20 hidden units (rel-
205 atively shallow). We find that increasing the number of layers does not improve the skill
206 of the model, and this architecture supports the interpretability of the fully connected
207 neural network for scientific discovery. In particular, we apply the Rectified Linear Unit
208 (ReLU; Agarap, 2018) activation function to all hidden layer nodes before the output
209 layer, which is defined as $f(x) = \max(0, x)$. ReLU is well equipped for use in LRP vi-
210 sualization, since it tests whether individual neurons have been activated (Toms et al.,
211 2020). We also apply a soft-max function to the output layer, which normalizes the decadal
212 class probabilities so that they add up to one. Both ReLU and soft-max functions are
213 common in ANN classification problems such as ours (e.g., Lecun et al., 2015; Goodfel-
214 low et al., 2016; Samek et al., 2020).

215 Before the maps are fed into the ANN, all training data are standardized by their
216 standard deviation across all ensemble members and years at each grid point. Each ANN
217 is then trained using a randomly selected subset of 80% of the climate model simulation
218 data (16 ensemble members) and tested on the remaining 20% (4 ensemble members).
219 During training, our loss function uses binary cross-entropy/log loss, which acts to pe-
220 nalize the ANN when the prediction is wrong, but the model confidence is still high. The
221 ANN are trained using the Nesterov method (momentum = 0.9) for stochastic gradient
222 descent (SGD; Ruder, 2016) for 500 epochs. While the interpretability results are not
223 sensitive to our selection in hyperparameters, we set our learning rate to 0.01 and a batch
224 size to 32 for each ANN used to generate the following figures.

225 To overcome the problem of overfitting the input data, we use L_2 ridge regulariza-
226 tion (Friedman, 2012). The L_2 parameter is set to 0.01 and applied to the weights of the
227 first hidden layer. L_2 regularization imposes a penalty on the model by adding a coef-
228 ficient to the loss function that is proportional to the sum of the squares of the feature
229 weights. Thus, L_2 regularization leads to weights that are more smoothly distributed across

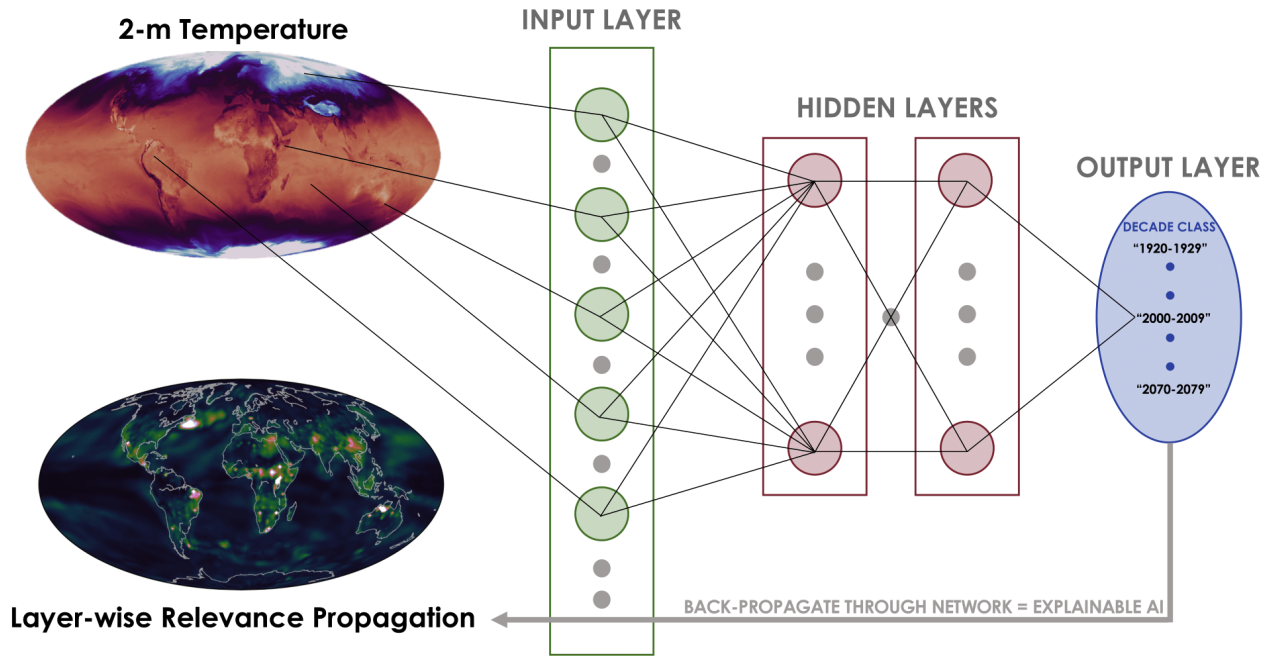


Figure 1. Schematic of the artificial neural network (ANN) used in this study for predicting the decade/year from global maps of 2-m air temperature (input layer). The shallow ANN features two hidden layers that both contain 20 hidden units. The output layer uses fuzzy classification (Zadeh, 1965) to assign each prediction year to the probability of it occurring in a single decade (e.g., within 2000-2009) (Barnes et al., 2020). An example heatmap using layer-wise relevance propagation (LRP; Bach et al., 2015) is also illustrated here. LRP highlights the regions of greater relevance for the ANN to predict the year by propagating an output sample backward through the frozen nodes of the ANN until it reaches the input layer (Toms et al., 2020). Thereby, LRP can attempt to learn the prediction decision by the ANN.

230 the model and are not as sensitive to outliers in the input data. Importantly, and in re-
 231 lation to standard climate science tools, the inclusion of this parameter accounts for spa-
 232 tial autocorrelation that can exist in the 2-m temperature fields. L_2 also improves the
 233 interpretation of the LRP heatmaps for identifying key regions that are relevant for the
 234 ANN to make its prediction (e.g., see Figure 3 in Barnes et al., 2020).

235 Finally, to retrieve the predicted year (output) by the ANN from the maps of 2-
 236 m temperature (input), we use a method called fuzzy classification encoding and decod-
 237 ing (Zadeh, 1965; Amo et al., 2004). This occurs during the ANN’s output layer (see Barnes
 238 et al. (2020)). From this approach, each decade is identified by its central year (e.g., 2005
 239 for 2000 to 2009). The ANN is then designed to assign an input map to the probabil-
 240 ity of it falling under a particular decade class (encode). Finally, fuzzy classification de-
 241 termines the particular year by computing the weighted sum of the decadal class prob-
 242 abilities (decode). For instance, the year 2008 would be encoded with the probability of
 243 0.7 of belonging to class center 2005 (for 2000 to 2009) and 0.3 of belonging to class cen-
 244 ter 2015 (for 2010 to 2019). Thus, we can compute the exact year as follows: $0.7 \cdot 2005 +$
 245 $0.3 \cdot 2015 = 2008$. Additional examples are depicted in Figure 2 of Barnes et al. (2020).
 246 Utilizing this setup, we hold onto each particular year while still performing a classifi-
 247 cation task for use in computing the LRP visualizations. Given our approach using both
 248 LRP and fuzzy classification, we do not explore the more typical method of multiple lin-
 249 ear regression in this work. However, that approach has been explored in Barnes et al.
 250 (2019, 2020) for CMIP temperature and precipitation data.

251 **2.4 Layer-wise Relevance Propagation**

252 The motivation for this work is to reveal the underlying climate patterns that are
 253 learned by the ANN from climate model simulations with different combinations of ex-
 254 ternal forcing. As we will show, using XAI tools alongside existing climate science meth-
 255 ods have the potential to bring new insights for interpreting projections of climate change
 256 in GCMs.

257 For this work, we use an interpretation method called layer-wise relevance prop-
 258 agation (LRP; Bach et al., 2015; Montavon et al., 2018) for tracing the decisions deter-
 259 mined by the ANN. While there are an increasing number of LRP routines, we use a form
 260 here (alpha-beta rule) that works well for ReLU networks and is related to Taylor se-

261 ries expansion (Montavon et al., 2017). By propagating information backward until the
 262 first layer of the ANN is reached, we learn about the individual input units (features)
 263 that are “relevant” to make the ANN’s prediction.

264 While a detailed overview of using LRP in the geosciences is provided in Toms et
 265 al. (2020), we briefly describe the method here: (1) the weights and biases of the ANN
 266 are frozen after training, (2) a single prediction output (prior to the soft-max function)
 267 is conserved and propagated backward through each node of the ANN based on the frozen
 268 weights and biases, (3) the feature relevance is learned until the propagation reaches the
 269 input layer, and (4) the final output of LRP retains the original dimensions of the in-
 270 put data by showing the relevance for each pixel (i.e., gridded latitude by longitude points
 271 on a map). This process is repeated for every sample. Hence, we are left with a spatial
 272 heatmap (unitless) showing the regions of importance for the ANN to determine the decade
 273 (see Figure 1).

274 In this study, our heatmaps are composites of both training and testing sample data.
 275 Since our output layer can return multiple probabilities of a 2-m temperature map oc-
 276 ccurring in a particular decade (fuzzy classification encoding and decoding), we only prop-
 277 agate the output value with the highest probability of belonging to a particular decade.
 278 Again, LRP can only propagate one sample backwards at a time. However, previous work
 279 has found that this does not affect the interpretation of the LRP output (Barnes et al.,
 280 2020). One final note about our use of LRP is that it only returns information that pos-
 281 itively contributes to the accuracy of the ANN prediction. Other XAI methods are ex-
 282 ploring ways to interpret negative weights and biases that contribute to less confident
 283 predictions (e.g., Botari et al., 2020), but that is beyond the scope of this analysis. To
 284 interpret the heatmap figures in this study, the higher relevance values indicate greater
 285 importance for the ANN’s prediction. Lastly, we introduce a method to mask noise (i.e.,
 286 relevance) in the LRP output (Section 3.2).

287 **3 Results**

288 **3.1 Response to External Forcing**

289 ***3.1.1 Evolution of simulated and observed trends***

290 We first evaluate the three large ensemble experiments (AER+, GHG+, ALL) us-
 291 ing more traditional climate science methods (i.e., trend analysis and signal-to-noise ra-

292 tios) to understand the spatial patterns of the 2-m temperature response. Figure 2 shows
293 annual maps of temperature trends over four separate 40-year periods for the ensemble
294 mean of each experiment. In the historical period, there is an observed cooling for AER+
295 (time-evolving aerosols; constant greenhouse gases) for all continental regions and most
296 of the world’s oceans (Figures 2a-2b). However, there is a notable statistically signifi-
297 cant region of warming over parts of the North Atlantic and Southern Ocean (Figure 2b).
298 These areas of warming may be connected to a strengthened Atlantic Meridional Over-
299 turning Circulation (AMOC) (Dagan et al., 2020; Keil et al., 2020; Menary et al., 2020).
300 The global signature of cooling prior to 2000 is associated with an increase in industrial
301 aerosol emissions. Trends in aerosol optical depth are driven by an increase in emissions
302 over Southeast Asia, North America, and Europe in the first half of the 20th century (see
303 Figure 2 in Deser, Phillips, et al., 2020). However, a decrease in aerosol optical depth
304 is observed in North America and Europe closer to present-day with the largest aerosol
305 forcing remaining over Southeast Asia. As industrial aerosols are reduced over the 21st
306 century, there is a net warming trend globally in AER+ through 2080 (Figure 2c-2d).
307 Notably, the temperature trend in the North Atlantic reverses and resembles the “North
308 Atlantic Warming Hole.” In agreement with earlier studies (e.g., Dagan et al., 2020), this
309 suggests an important role for aerosols in North Atlantic climate variability. Figure 2e-
310 2h reveals the global warming signature due to the dominant greenhouse gas forcing in
311 GHG+ (time-evolving greenhouse gases; constant aerosols), along with a cooling patch
312 in the North Atlantic. Relative to GHG+, statistically significant warming trends emerge
313 later in ALL (Figure 2i), which is due to its greater aerosol forcing prior to 1960 (net
314 cooling effect). As trends in optical aerosol depth decrease by 2040, there are larger global
315 temperature trends in ALL (Figure 2l) compared to GHG+ (Figure 2h).

316 We compare the simulated temperature trends with observations by showing the
317 observed (using 20CRv3) 2-m temperature trend (annual mean) for two 40-year peri-
318 ods in Figure S1. However, we note that the observations reflect only one possible re-
319 alization of internal variability. Therefore, they are not directly comparable with the en-
320 semble mean trends presented in Figure 2. Regardless, we still find some common tem-
321 perature signatures emerge. By the second half of the 20th century (Figure S1b), we find
322 statistically significant warming across the majority of the tropics and parts of North
323 America. We also find the cooling trend over the North Atlantic detectable in observa-
324 tions for the 1960 to 1999 period.

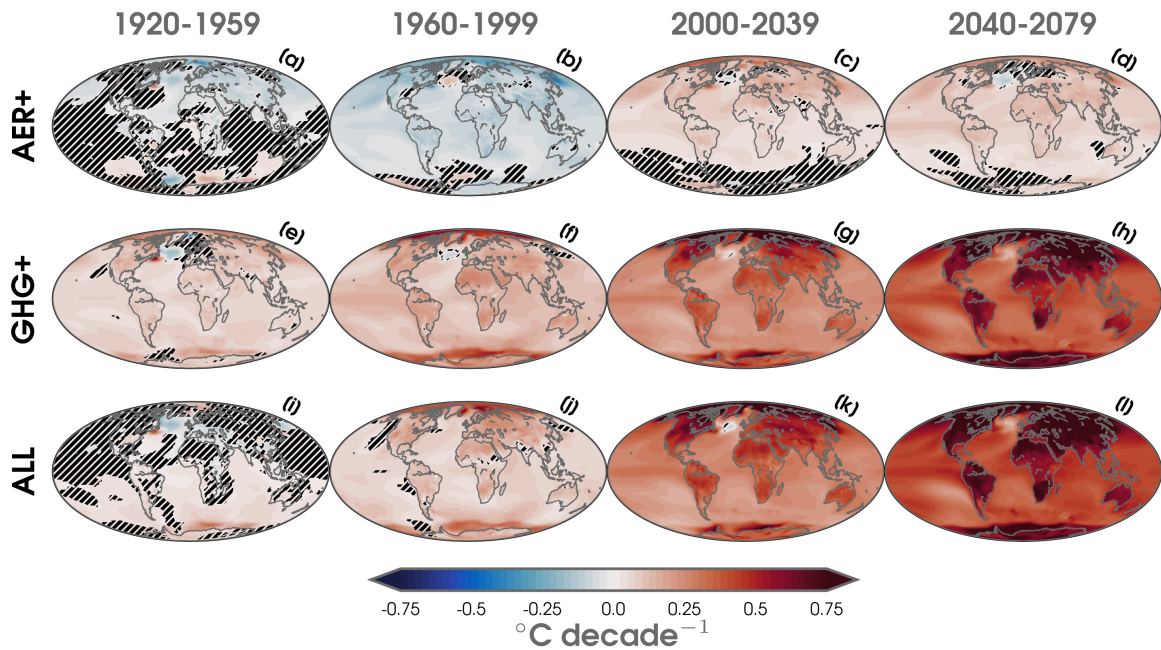


Figure 2. Annual linear least squares trends of 2-m temperature ($^{\circ}\text{C}$ per decade) over 1920 to 1959 (a,e,i), 1960 to 1999 (b,f,j), 2000 to 2039 (c,g,k), and 2040 to 2079 (d,h,l) for the ensemble means of three climate model simulations (AER+; a-d, GHG+; e-h, ALL; i-l). Statistically significant trends are shown with shaded contours at the 95% confidence level following the Mann-Kendall (MK) test (Mann, 1945; Bevan & Kendall, 1971), while those that are not are masked out using black hatch marks.

325 To understand the timing of emergence of forced climate signals, we compute signal-
326 to-noise (SNR) maps in Figure S2. Here, the SNR is computed as the absolute ensem-
327 ble mean trend divided by the standard deviation of the individual ensemble member
328 trends for each 40-year period. We observe the highest SNR in the tropics, which is a
329 result of the smaller internal variability in this region. High values of SNR (> 3) emerge
330 as early as the 1920 to 1959 period in GHG+ from the Amazon to the Indian Ocean (Fig-
331 ure S2e), but do not appear until the later half of the 20th century in ALL (Figure S2j-
332 S2k). SNR values are also high in the tropics for the AER+ simulation, but there is lit-
333 tle to no forced response (SNR < 1) in the extratropics and polar regions (Figure S2a-
334 S2d). While the global warming signal overwhelms internal variability in GHG+ and ALL
335 beginning in the 2000 to 2039 period, SNR values remain lower ($\sim 1-2$) in the subpolar
336 Atlantic.

337 The effect of aerosols has a consequential role in identifying patterns of forced cli-
338 mate signals. Increases in industrial aerosol loading (e.g., prior to 1960) can mask the
339 timing of emergence of greenhouse gas-induced warming, particularly in the extratrop-
340 ics (Figure S2). Therefore, to fully understand the patterns of responses that are driven
341 by anthropogenic climate drivers, we now turn to our interpretable ANN architecture.
342 One advantage to using our ANN is that we can address potential nonlinearities in re-
343 gional responses that evolve over time, which would not be captured in the simple trend
344 and SNR analysis.

345 ***3.1.2 Predictions by the ANN***

346 Figure 3 shows the predictions by the ANN after separately training and testing
347 on each of the three large ensemble experiments. Here, we use fuzzy classification de-
348 coding to show how well the ANN can predict the year from the input maps of 2-m tem-
349 perature. It is clear that the ANN closely predicts the year on the climate model data,
350 especially after 1980 (blue shading). This is particularly noticeable in ALL (Figure 3c),
351 where the ANN is not able to discern the year in the first half of the 20th century. We
352 also note that the ANN performs even better in AER+ compared to ALL for training
353 and testing, despite the fact that there is no time-evolving greenhouse gas forcing and
354 consequently smaller global mean temperature trends.

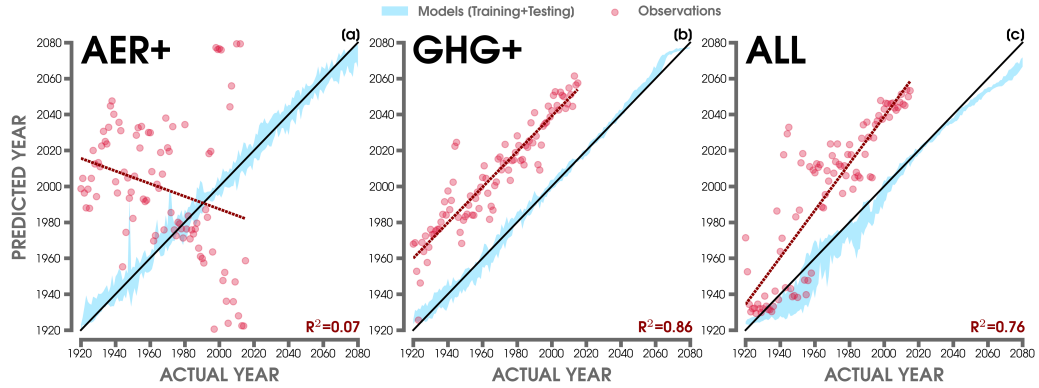


Figure 3. (a) Predictions of the year by the artificial neural network (y-axis) compared to the actual year (x-axis) from global maps of annual 2-m temperature in AER+. (b) Same as (a) but for GHG+. (c) Same as (a) but for ALL. The blue shading highlights the 5th-95th percentiles of predictions from the combined training and testing large ensemble data. The red points show the ANN predictions using 20CRv3 observations. The red dashed line shows the linear least squares fit through the predicted observations in each model, and the associated R^2 is shown in the lower right-hand corner. The 1:1 line (or perfect prediction) is overlaid in black.

355 To assess the utility of our ANNs that are trained only on climate model data, we
 356 test their performance on observations by inputting 2-m temperature maps from 20CRv3.
 357 By testing on observational data, we find striking differences between the ANN predic-
 358 tions. The ANN has no skill in predicting the year for observations after training on AER+
 359 (Figure 3a). Since the real world features a large greenhouse gas-induced warming sig-
 360 nal, the ANN does not learn regional indicators that are in common with observations.
 361 The ANN also performs worse on observations for the ALL model prior to 1980 (Fig-
 362 ure 3c). Considering that a forced temperature response has not clearly emerged from
 363 the background noise (see Figure S2i-S2j), we infer that this is why the ANN is unable
 364 to detect the year.

365 In contrast, the ANN performs quite well after training on GHG+ for predicting
 366 the order of the years in observations (Figure 3b). Since the real world does consist of
 367 both direct and indirect effects of greenhouse gases and aerosols, it is somewhat surpris-
 368 ing to see that the ANN trained on GHG+ performs better on predicting the year in ob-
 369 servations than ALL. In fact, the observations approximately parallel the 1:1 line in GHG+,
 370 but are offset by about four decades. This means that the patterns of forced responses

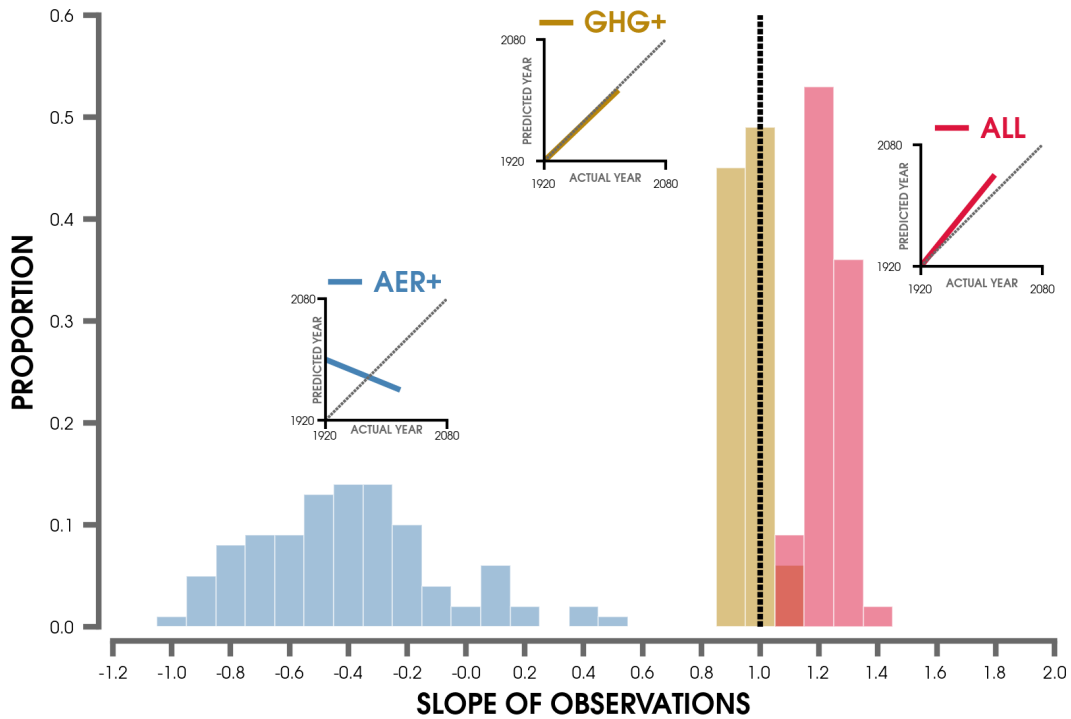


Figure 4. Histogram of the possible slopes of predicted 20CRv3 observations after considering different combinations of training and testing data for each of the AER+ (blue), GHG+ (brown), and ALL (red) artificial neural networks. An example graph of the median slope of predicted observations is shown next to every histogram for the actual year (x-axis) relative to the predicted year (y-axis) (similar to Figure 3). The 1:1 is highlighted by the dashed gray lines.

371 are similar, but may emerge later in the climate model data compared to observations.
 372 This offset could also arise from a difference in Earth’s mean temperature that is com-
 373 mon between climate models and reanalysis data sets (Hawkins & Sutton, 2016). There-
 374 fore, we compare our results in Figure 3 to ANNs trained using input data with the global
 375 mean temperature removed from each map (not shown). The results are quite similar.
 376 The ANN is still more skillful in predicting the year of the observations on the ANN trained
 377 using GHG+. This evidence suggests that the ANN is learning regional temperature sig-
 378 nals and not just differences in the global mean temperature to make its predictions, as
 379 discussed further in Section 3.3.

380 We investigate the robustness of our observational predictions in Figure 3 by us-
 381 ing 100 unique ANNs trained on different combinations of training and testing data sets
 382 (i.e., individual ensemble members). We then test our observational data on each of these
 383 100 iterations and plot a histogram of their predicted (linear) slopes in Figure 4. In agree-
 384 ment with our single trained ANNs in Figure 3, we find that the observations tested on
 385 the ANN using GHG+ performs the closest to the 1:1 (or perfect prediction) line with
 386 little variability between each iteration. Once again, there is no skill in predicting the
 387 year of the observations for the ANN trained on the AER+ simulation. In ALL, the me-
 388 dian slope is greater than the 1:1 line likely due to the fact that a forced temperature
 389 signal does not emerge until after the middle of the 20th century.

390 While the results in Figures 3 and 4 show predictions based on maps of annual mean
 391 2-m temperature, we also investigate differences by calculating seasonal means before
 392 training and testing the ANN. Figure S3 show the results of predicting the year for bo-
 393 real winter (January-February-March; JFM) and boreal summer (July-August-September;
 394 JAS) in the ANNs using GHG+ and ALL+, respectively. Once more, we find that the
 395 predicted year of the observations is improved by testing on the GHG+ model. Notably,
 396 we also find a slight improvement in ANN skill (both GHG+ and ALL) on observations
 397 from JAS relative to JFM. This may be a result of greater internal variability of 2-m tem-
 398 peratures in the Northern Hemisphere during JFM. In other words, the indicator pat-
 399 terns in common between observations and the climate model data may be weaker in bo-
 400 real winter compared to summer.

401 To understand how the ANN is making its predictions, we utilize LRP for evalu-
 402 ating regional climate patterns of interest. In particular, we investigate why the ANN
 403 predictions of observations appear more accurate after training on a climate simulation
 404 without time-evolving aerosols. As a reminder, the LRP heatmaps indicate areas of “rel-
 405 evance” (or importance) for the ANN to make an accurate prediction. Therefore, greater
 406 relevance does not necessarily correspond to the locations of greatest climate forcing. Ad-
 407 ditionally, the locations of higher relevance may change over time.

408 **3.2 Uncertainty in Layer-wise Relevance Propagation**

409 The LRP algorithm employed here provides output (relevance) for all grid points
 410 of every sample. However, it can be difficult to distinguish physically meaningful regions

411 of importance to the ANN, especially for identifying known climate signals. To limit noise
412 in our LRP maps, we compute a threshold (or statistical significance) using a baseline
413 relevance value. In other words, we determine the maximum feature relevance that could
414 be expected from an ANN that is trained on random noise. While other uncertainty met-
415 rics for LRP have been proposed (e.g., Bykov et al., 2020; Fabi & Schneider, 2020), our
416 simple method can be employed without modifying the existing ANN architecture or LRP
417 algorithm and takes a common approach applied by climate scientists.

418 We compute this baseline relevance threshold as follows: (1) we randomly shuffle
419 the individual ensemble member and year dimensions of the ALL input data while keep-
420 ing the true year fixed (not shuffling), (2) we proceed with training and testing using the
421 same ANN architecture and hyperparameters as Section 2.3, (3) each output sample is
422 then propagated backward into the ANN to compute the relevance map, (4) we repeat
423 steps 1-3 for 500 iterations of the ANN by using unique random initialization seeds and
424 taking different combinations of the training and testing data, and (5) finally, we com-
425 pute the 95th percentile from the distribution of LRP values at all grid points that are
426 obtained from this procedure. Thus, this bootstrapping-like method determines the dis-
427 tribution of LRP values that could be expected from climate data with no serial auto-
428 correlation or temporal trends from forced signals.

429 Figure 5 displays a histogram of this distribution of LRP values after 500 unique
430 iterations of the shuffled ANN. We also test our observations (20CRv3) on the ANN trained
431 by the shuffled ensemble from steps (1)-(5). As expected, the ANN cannot predict the
432 year (median linear slope near 0), since it is unable to learn any forced climate signals
433 from the shuffled data. Figure S4 shows a histogram of possible R^2 values from the lin-
434 ear fit of observations compared to the median R^2 of observations trained on either AER+,
435 GHG+, or ALL (Section 3.1.2). We also show an example of a LRP map from a single
436 iteration of the ANN trained on the shuffled ensemble, which highlights the lack of rel-
437 evant regions for the ANN to make a decision on this synthetic data.

438 As an additional check of our methodology, we create a “large ensemble” of ran-
439 dom numbers drawn from a normal distribution. This large ensemble of random noise
440 has the same dimensions as our real data (20 ensembles, 161 years, 96 by 144 spatial grid
441 points). After repeating steps (2)-(5), we find that the 95th percentile of the random noise
442 LRP is in close agreement with our baseline calculated from Figure 5 (not shown).

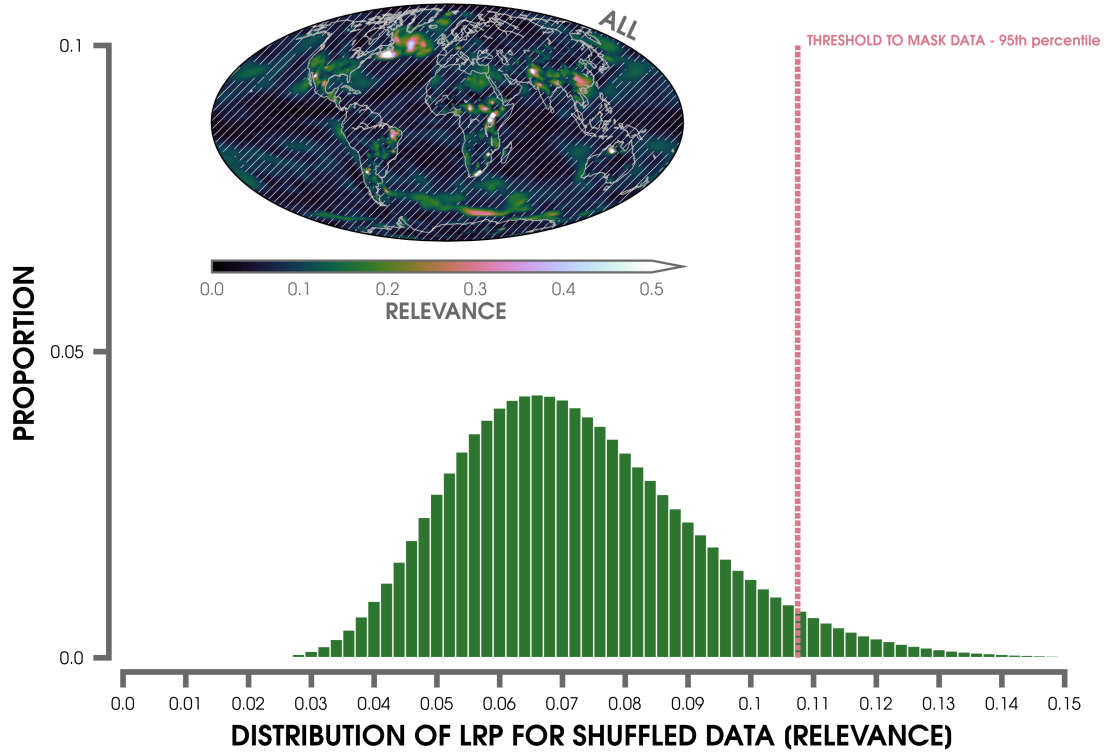


Figure 5. Histogram of the possible relevance values from layer-wise relevance propagation (LRP) after randomly shuffling the ensemble members and years of the input data using the ALL experiment. The 95th percentile LRP threshold is shown by the dashed vertical red line. The LRP composite heatmap is shown for the ALL experiment (training and testing data) using each year from 1920 to 2080 after masking out (white hatch marks) statistically insignificant values (i.e., below the LRP threshold from the histogram; see text for details). Higher LRP values indicate greater relevance for the artificial neural network’s prediction.

3.3 Regions of Climate Signal

Figure 6 show the LRP heatmaps for the individual ANN’s trained on AER+, GHG+, and ALL input data of annual mean 2-m temperature. Our LRP maps are averaged for every prediction sample (ensemble member) that is accurate to within ± 2 years of the actual year (Barnes et al., 2020). In Figure 6, we show the temporal evolution of relevance for the four periods we have considered in this study (e.g., Figure 2). These LRP maps are composites after masking out the relevance below our new uncertainty threshold (see Figure 5). To compare the influence of our LRP uncertainty metric introduced in Section 3.2, we also show the same LRP heatmaps in Figure S5, but without using a mask. Comparing Figure 6 to Figure S5, we now see several climate regions of interest (e.g., North Atlantic and Southeast Asia) that are more clearly distinguishable from the background noise.

The North Atlantic is a key region of relevance between all three large ensembles, but is largest in GHG+ during the 1960 to 2039 period (Figure 6g). The LRP maps also reveal Southeast Asia as an important region for the AER+ and ALL neural networks. The relevance is largest in Southeast Asia for AER+ during the early 20th (Figure 6a) and early 21st centuries (Figure 6c). Again, although the regions of relevance do not directly correspond to surface forcing, we infer that the emissions of anthropogenic aerosols over Southeast Asia and India are important indicators for the ANN to predict the year in the AER+ and ALL large ensembles. We also find that the Southern Ocean is a significant region of relevance for the large ensembles that observe time-evolving greenhouse gases (GHG+ and ALL). Notably, this Southern Ocean signal appears along the Antarctic sea-ice edge. However, in agreement with Barnes et al. (2020), we find that the Arctic is not a region of importance for predicting the year in any of the large ensemble simulations. Despite the effects of Arctic amplification, the lack of relevance to the ANN prediction is likely a result of the large atmospheric internal variability in the high latitudes relative to the tropics (Figure S2).

To compare the differences in LRP maps between seasonal and annual mean input data, we show their relevance composites over 1960 to 2039 in Figure 7. This period is selected due to the greater differences in the timing of emergence of forced signals between the three large ensembles (Section 3.1.1). For the LRP maps based on the annual mean data (Figures 7a,f,k), we observe higher relevance in the North Atlantic for

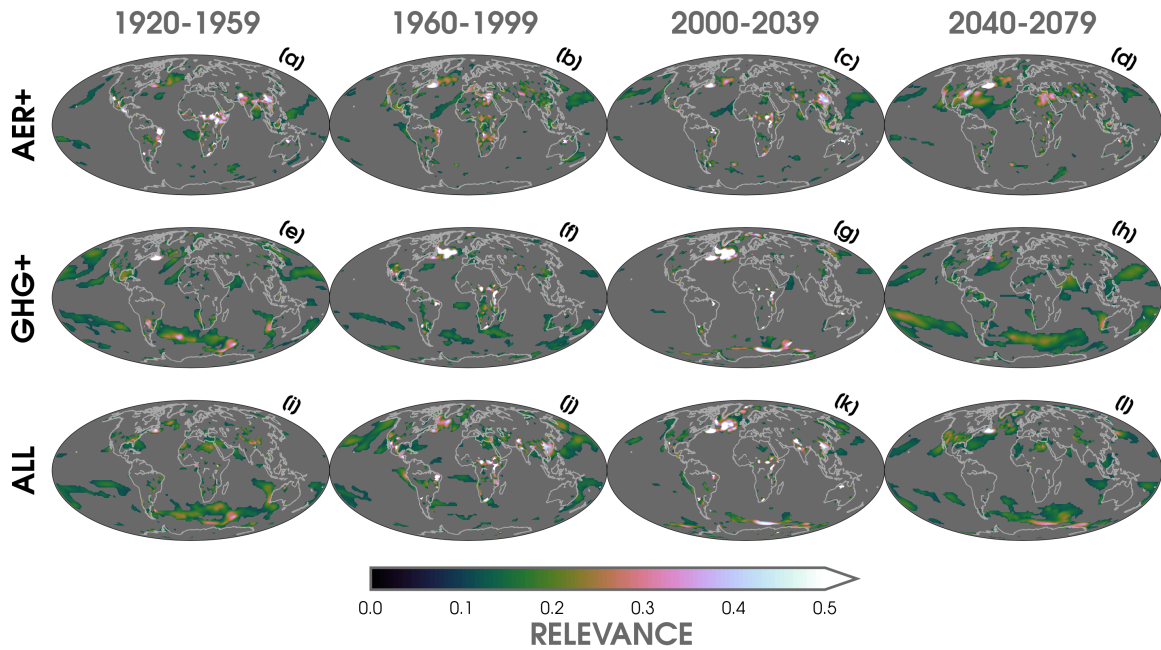


Figure 6. Layer-wise relevance propagation (LRP) composite heatmaps averaged over 1920 to 1959 (a,e,i), 1960 to 1999 (b,f,j), 2000 to 2039 (c,g,k), and 2040 to 2079 (d,h,l) for the three large ensemble experiments (AER+; a-d, GHG+; e-h, ALL; i-l). Higher LRP values indicate greater relevance for the artificial neural network’s prediction. Relevance values less than the 95th percentile threshold (see text) have been masked out (gray shading).

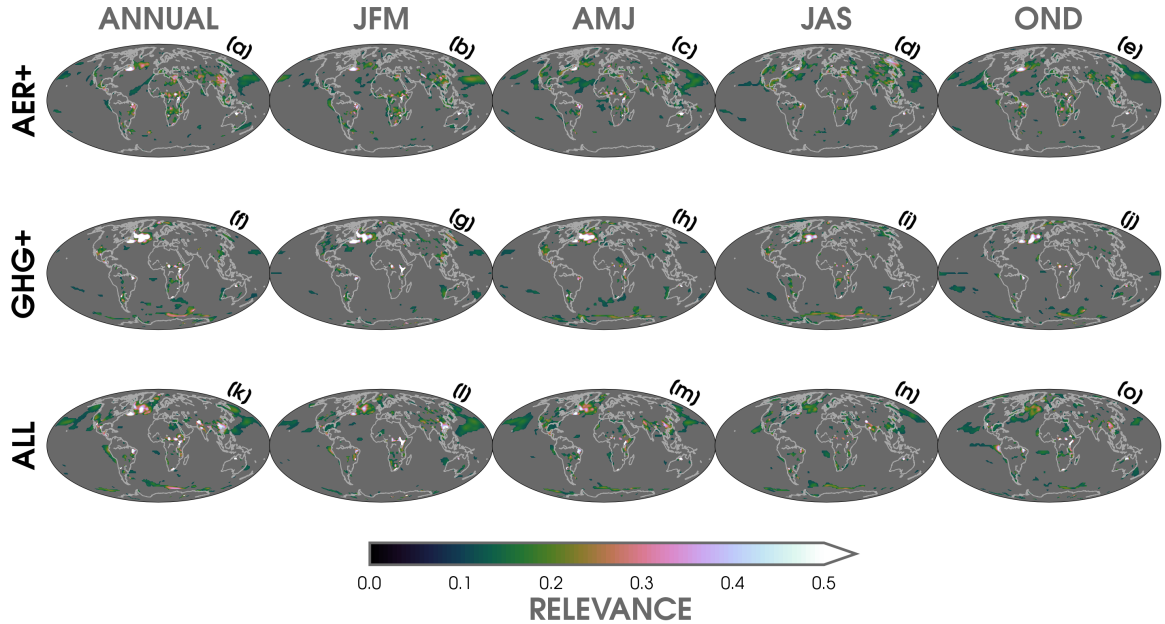


Figure 7. Layer-wise relevance propagation (LRP) heatmaps for ANNs trained separately on annual (a,f,k), January-March (JFM; b,g,l), April-June (AMJ; c,h,m), July-September (JAS; d,i,n), and October-December (OND; e,j,o) input data of 2-m temperature using the three large ensemble experiments (AER+; a-e, GHG+; f-j, ALL; k-o). Every LRP map is composited over the 1960 to 2039 period for the annual data and in each season. Higher LRP values indicate greater relevance for the ANN’s prediction. Relevance values less than the 95th percentile threshold (see text) have been masked out (gray shading).

475 AER+, GHG+, and ALL neural networks. This area of relevance is largest in the ANN
 476 trained on GHG+ and is somewhat consistent between seasons. In agreement with Fig-
 477 ure 6, this shows that the North Atlantic is a particularly important region for the neu-
 478 ral network to predict the year. For AER+ and ALL, we observe a relevance hotspot over
 479 India and Southeast Asia, which is distinct during JFM and OND. This is likely due to
 480 the local influence of time-evolving aerosols in these climate model simulations, which
 481 are absent in the ANN trained on GHG+. Although there are some regional and sea-
 482 sonal differences in Figure 7, the primary climate indicators (“relevance hotspots”) re-
 483 main similar. Thus, we focus on the annual mean input data for the rest of our analy-
 484 sis.

485 As previously discussed (e.g., in Figure 4), we test the robustness of our results by
 486 running 100 unique iterations of each large ensemble ANN for different combinations of
 487 training and testing data. Figure S6 shows a composite LRP heatmap that is averaged
 488 over all 100 possible iterations of the ANN for only the mean 1960 to 2039 period. The
 489 regions of greatest relevance are consistent with Figure 7 and point to the North Atlantic
 490 and portions of Southeast Asia (only in AER+ and ALL) as essential to the ANN’s pre-
 491 dictions. This highlights that the regional signals are robust, even after considering dif-
 492 ferent combinations of individual ensemble members. Moreover, the patterns of higher
 493 relevance are also similar when averaging across all climate model years (1920-2080; Fig-
 494 ure 5).

495 Figure 8 shows the distribution of relevances from the 100 unique ANN iterations
 496 for the mean relevance value (1960-2039) in five regions (Southeast Asia, India, North
 497 Atlantic, Central Africa, and a portion of the Southern Ocean). The small variance in
 498 all of the distributions further reinforces the importance of these areas as key climate
 499 indicator patterns that are learned by our nonlinear ANN. We find weaker relevance over
 500 Southeast Asia (Figure 8a) and India (Figure 8b) for GHG+, which is likely a result of
 501 its industrial aerosols being held fixed to 1920 levels. Thus, the temperature signals in
 502 these regions (e.g., absence of local cooling due to aerosols) are not as important for the
 503 ANN prediction. In contrast, GHG+ observes the greatest relevance in the North At-
 504 lantic, while AER+ observes the smallest relevance in this same area (Figure 8c). In-
 505 terestingly, the North Atlantic distribution for ALL falls between AER+ and GHG+.
 506 The relevance signals across Central Africa (Figure 8d) and the Southern Ocean (Fig-
 507 ure 8e) are mostly consistent between large ensemble simulations. Nevertheless, we note
 508 that there is a slight tendency for the Southern Ocean to be more important for the ANN
 509 when there is a larger relative contribution from greenhouse gas forcing (GHG+ and ALL).
 510 These LRP results highlight the key importance of the North Atlantic and Southeast Asia
 511 for the ANNs to make their predictions.

512 Finally, to understand where the ANN focuses its attention when making predic-
 513 tions on real world data, Figure 9 shows LRP maps for the observations that are input
 514 into the ANNs. Similar to the previous LRP maps of the climate model training and test-
 515 ing data, we find several common relevance regions emerge (e.g., North Atlantic and South-
 516 east Asia). However, recall that the prediction of the years for observations are strikingly
 517 different between each large ensemble ANN (Figure 3). In particular, the GHG+ neu-

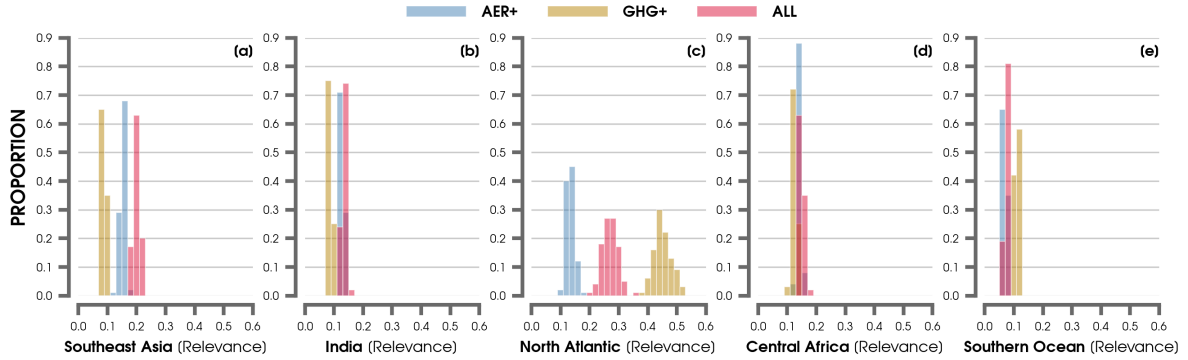


Figure 8. Histograms of mean relevance from layer-wise relevance propagation (LRP) over Southeast Asia (a), India (b), the North Atlantic warming hole region (c), Central Africa (d), and the Southern Ocean (e) for 100 unique iterations of the AER+ (blue), GHG+ (brown), and ALL (red) models. Mean LRP values are averaged over each year from 1960 to 2039.

518 ral network is more skillful in predicting the order of the years than by ALL. While there
 519 is somewhat greater relevance using observations across the North Atlantic and South-
 520 ern Ocean for the ANN trained on GHG+ (Figure 9c-9d) compared to ALL (Figure 9e-
 521 9f), the general patterns between the LRP maps are similar. This indicates that the neu-
 522 ral networks are learning different combinations of these regional temperature signals to
 523 predict the observations. This also suggests that the GHG+ network may be more skill-
 524 ful by focusing on greenhouse gas-induced responses that are closer to real world data,
 525 rather than the temperature patterns which are modulated by industrial aerosol forc-
 526 ing in the AER+ and ALL large ensembles. Hence, the LRP maps reveal how industrial
 527 aerosols can either mask or augment detection of greenhouse gas-induced warming sig-
 528 nals on local to regional scales.

529 4 Discussion and Conclusions

530 Due to complex interactions between internal and external forcings in the climate
 531 system, it remains difficult to estimate the local and regional influence of human-induced
 532 climate change on surface air temperatures (Schneider & Held, 2001; Deser et al., 2012;
 533 McKinnon & Deser, 2018). Our work demonstrates the utility of explainable artificial
 534 intelligence (XAI) methods for extracting patterns of climate signals due to varying ex-
 535 ternal forcing, which adds to an existing set of statistical techniques for evaluating signal-

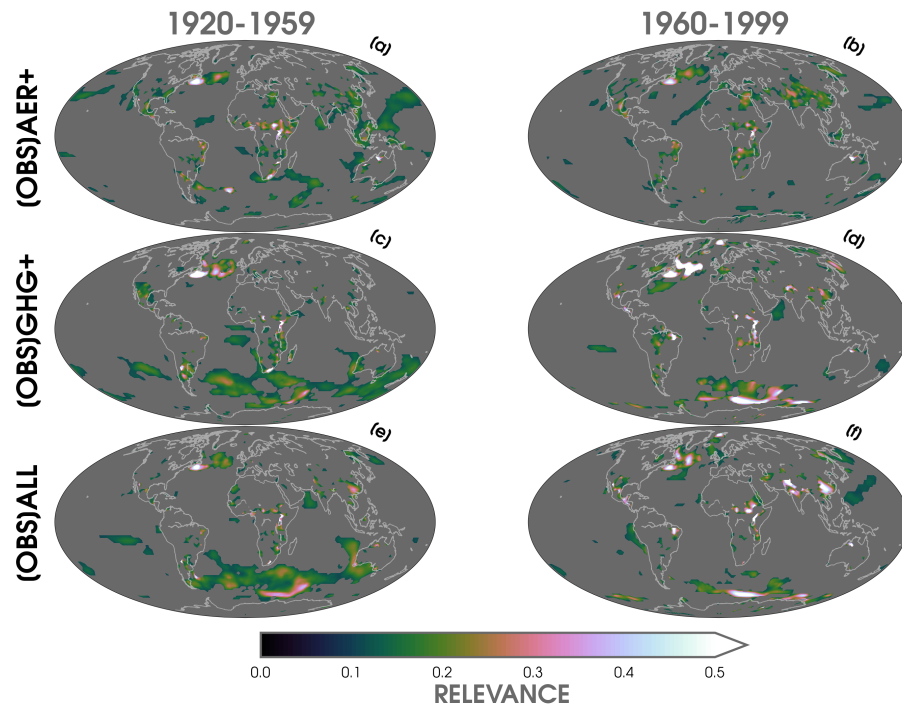


Figure 9. Layer-wise relevance propagation (LRP) composite heatmaps (annual mean) averaged over 1920 to 1959 (a,c,e) and 1960 to 1999 (b,d,f) for observations (OBS) tested separately on each large ensemble ANN (AER+; a-b, GHG+; c-d, ALL; e-f). Higher LRP values indicate greater relevance for the artificial neural network’s prediction. Relevance values less than the 95th percentile threshold (see text) have been masked out (gray shading).

536 to-noise in the Earth system (e.g., Wills, Sippel, & Barnes, 2020). By leveraging a XAI
537 tool as a novel pattern recognition method, we aim to understand how a nonlinear ar-
538 tificial neural network (ANN) makes a prediction by learning regional climate signals.

539 We build off of ANN results from Barnes et al. (2019, 2020) by investigating the
540 role of different anthropogenic external forcings on temperature patterns relative to the
541 influence of atmospheric internal variability. Using climate model data from a new set
542 of large ensemble experiments, we compare different combinations of human-induced cli-
543 mate drivers (greenhouse gases and industrial aerosols) on forced temperature signals
544 over the 20th and 21st centuries. The large number of ensemble members from one fully-
545 coupled climate model (CESM1) allow us to disentangle forced changes from internal vari-
546 ability. In particular, we use layer-wise relevance propagation (LRP) to investigate how
547 the ANN learns regional climate patterns in order to predict the year from inputs of 2-
548 m air temperatures. Importantly, LRP allows us to investigate the time-evolving rele-
549 vance (from 1920 to 2080) of input features (maps of 2-m temperature) for the ANN to
550 make an accurate prediction. We also introduce a simple metric to further extract the
551 key relevance regions from the LRP maps. Lastly, we test our nonlinear ANN on obser-
552 vations from a new 20th century atmospheric reanalysis data set (20CRv3) in order to
553 understand how the effect of different external climate forcings impact the prediction of
554 our ANN after testing on real world data.

555 While efforts are underway to constrain observational uncertainties for the effec-
556 tive radiative forcing of aerosols (e.g., Yoshioka et al., 2019; Bellouin et al., 2020; Ben-
557 der, 2020; C. Smith et al., 2020), the net influence of aerosols on regional temperature
558 variability remains highly uncertain in historical and future climate model simulations
559 (Bauer et al., 2020; Dittus et al., 2020; Peace et al., 2020). Surprisingly, we found that
560 our ANN trained on a climate model simulation with fixed industrial aerosols (set to 1920
561 levels; GHG+) made the most accurate predictions after testing on real world observa-
562 tions of temperature. In contrast, the ANN trained on a large ensemble with the most
563 realistic external forcing configuration (ALL) was unable to make an accurate predic-
564 tion for observations until after the mid-20th century. The LRP maps based on obser-
565 vations indicate that the temperature signal in the North Atlantic is particularly rele-
566 vant for the more skillful predictions by the ANN trained on GHG+ compared to ALL.

567 Our ANN results suggests that CESM1 is highly sensitive to combinations between
 568 external forcings when simulating the variability and timing of emergence of global cli-
 569 mate signals, such as the North Atlantic Warming Hole, compared to observations. While
 570 we focus on only one set of single-forcing large ensembles, we recommend that additional
 571 experiments are conducted to fully understand the sensitivity of GCMs to aerosol radia-
 572 tive forcing and subsequently simulate realistic temperature trends and variability.

573 **Acknowledgments**

574 This work was supported by NOAA MAPP grant NA19OAR4310289. We would also
 575 like to acknowledge the CESM Large Ensemble Community Project and CISL supercom-
 576 puting resources provided by NCAR (doi:10.5065/D6RX99HX). Support for the 20CRv3
 577 dataset is provided by the U.S. Department of Energy (DOE) Office of Science Biolog-
 578 ical and Environmental Research (BER), by the NOAA CPO, and by the NOAA PSL.

579 **Data Availability Statements**

580 The CESM1 Large Ensemble simulations used in this study are freely available ([https://](https://www.cesm.ucar.edu/projects/community-projects/LENS/data-sets.html)
 581 www.cesm.ucar.edu/projects/community-projects/LENS/data-sets.html). Monthly
 582 20th Century Reanalysis V3 (20CRv3) data are provided by the NOAA/OAR/ESRL PSL,
 583 Boulder, Colorado, USA, from their website at <https://psl.noaa.gov/>. Monthly re-
 584 analysis data for ERA5 are also freely available available ([https://climate.copernicus](https://climate.copernicus.eu/climate-reanalysis)
 585 [.eu/climate-reanalysis](https://climate.copernicus.eu/climate-reanalysis)). Figures and data analysis were completed using Python v3.7.6,
 586 Numpy v1.19 (Harris et al., 2020), SciPy v1.4.1 (Virtanen et al., 2020), Matplotlib v3.2.2
 587 (Hunter, 2007), and colormaps provided by cmocean v2.0 (Thyng et al., 2016). Addi-
 588 tional Python packages used for development of the ANN and LRP visualizations include
 589 Keras/TensorFlow (Abadi et al., 2016) and iNNvestigate (Alber et al., 2019). References
 590 for the data sets are provided throughout the study.

591 **References**

- 592 Abadi, M., Barham, P., Chen, J., Chen, Z., Davis, A., Dean, J., . . . Zheng, X.
 593 (2016). TensorFlow: A system for large-scale machine learning. In *Proceedings*
 594 *of the 12th usenix symposium on operating systems design and implementation,*
 595 *osdi 2016*.
- 596 Agarap, A. F. (2018, mar). Deep Learning using Rectified Linear Units (ReLU).

- 597 *arXiv*. Retrieved from <http://arxiv.org/abs/1803.08375>
- 598 Alber, M., Lapuschkin, S., Seegerer, P., Hägele, M., Schütt, K. T., Montavon, G., ...
599 Kindermans, P. J. (2019). INNvestigate neural networks! *Journal of Machine*
600 *Learning Research*, 20.
- 601 Allen, R. J., & Sherwood, S. C. (2011, may). The impact of natural versus an-
602 thropogenic aerosols on atmospheric circulation in the Community Atmo-
603 sphere Model. *Climate Dynamics*, 36(9-10), 1959–1978. Retrieved from
604 <https://link.springer.com/article/10.1007/s00382-010-0898-8> doi:
605 10.1007/s00382-010-0898-8
- 606 Amo, A., Montero, J., Biging, G., & Cutello, V. (2004, jul). Fuzzy classification sys-
607 tems. *European Journal of Operational Research*, 156(2), 495–507. doi: 10
608 .1016/S0377-2217(03)00002-X
- 609 Bach, S., Binder, A., Montavon, G., Klauschen, F., Müller, K. R., & Samek, W.
610 (2015, jul). On pixel-wise explanations for non-linear classifier decisions by
611 layer-wise relevance propagation. *PLoS ONE*, 10(7), e0130140. Retrieved from
612 <http://www.hfsp.org/>, doi: 10.1371/journal.pone.0130140
- 613 Barnes, E. A., Hurrell, J. W., Ebert-Uphoff, I., Anderson, C., & Anderson, D. (2019,
614 nov). Viewing Forced Climate Patterns Through an AI Lens. *Geophysical Re-*
615 *search Letters*, 46(22), 13389–13398. Retrieved from <https://onlinelibrary>
616 [.wiley.com/doi/abs/10.1029/2019GL084944](https://onlinelibrary.wiley.com/doi/abs/10.1029/2019GL084944) doi: 10.1029/2019GL084944
- 617 Barnes, E. A., Toms, B., Hurrell, J. W., Ebert-Uphoff, I., Anderson, C., & Ander-
618 son, D. (2020, sep). Indicator Patterns of Forced Change Learned by an
619 Artificial Neural Network. *Journal of Advances in Modeling Earth Systems*,
620 12(9). Retrieved from [https://onlinelibrary.wiley.com/doi/10.1029/](https://onlinelibrary.wiley.com/doi/10.1029/2020MS002195)
621 [2020MS002195](https://onlinelibrary.wiley.com/doi/10.1029/2020MS002195) doi: 10.1029/2020MS002195
- 622 Bauer, S. E., Tsigaridis, K., Faluvegi, G., Kelley, M., Lo, K. K., Miller, R. L., ...
623 Wu, J. (2020, aug). Historical (1850–2014) Aerosol Evolution and Role on
624 Climate Forcing Using the GISS ModelE2.1 Contribution to CMIP6. *Journal*
625 *of Advances in Modeling Earth Systems*, 12(8). Retrieved from [https://](https://agupubs.onlinelibrary.wiley.com/doi/full/10.1029/2019MS001978)
626 agupubs.onlinelibrary.wiley.com/doi/full/10.1029/2019MS001978 doi:
627 10.1029/2019MS001978
- 628 Bellouin, N., Quaas, J., Gryspeerdt, E., Kinne, S., Stier, P., Watson-Parris, D., ...
629 Stevens, B. (2020, mar). *Bounding Global Aerosol Radiative Forcing of Climate*

- 630 *Change* (Vol. 58) (No. 1). Blackwell Publishing Ltd. Retrieved from [https://](https://agupubs.onlinelibrary.wiley.com/doi/full/10.1029/2019RG000660)
631 agupubs.onlinelibrary.wiley.com/doi/full/10.1029/2019RG000660 doi:
632 10.1029/2019RG000660
- 633 Bender, F. A. (2020). Aerosol Forcing: Still Uncertain, Still Relevant. *AGU Ad-*
634 *vances*, 1(3). doi: 10.1029/2019av000128
- 635 Beucler, T., Rasp, S., Pritchard, M., & Gentine, P. (2019, jun). Achieving Conserva-
636 tion of Energy in Neural Network Emulators for Climate Modeling. *arXiv*. Re-
637 trieved from <http://arxiv.org/abs/1906.06622>
- 638 Bevan, J. M., & Kendall, M. G. (1971). Rank Correlation Methods. *The Statisti-*
639 *cian*. doi: 10.2307/2986801
- 640 Bonfils, C. J., Santer, B. D., Fyfe, J. C., Marvel, K., Phillips, T. J., & Zimmer-
641 man, S. R. (2020). Human influence on joint changes in temperature,
642 rainfall and continental aridity. *Nature Climate Change*, 10(8). doi:
643 10.1038/s41558-020-0821-1
- 644 Booth, B. B., Harris, G. R., Jones, A., Wilcox, L., Hawcroft, M., & Carslaw, K. S.
645 (2018). *Comments on "Rethinking the lower bound on aerosol radiative forc-*
646 *ing"* (Vol. 31) (No. 22). doi: 10.1175/JCLI-D-17-0369.1
- 647 Botari, T., Hvilshøj, F., Izbicki, R., & de Carvalho, A. C. P. L. F. (2020, sep). Me-
648 LIME: Meaningful Local Explanation for Machine Learning Models. *arXiv*.
649 Retrieved from <http://arxiv.org/abs/2009.05818>
- 650 Boukabara, S.-A., Krasnopolsky, V., Penny, S. G., Stewart, J. Q., & MCGovern,
651 A. (2020). Outlook for Exploiting Artificial Intelligence in the Earth
652 and Environmental Sciences *. *Bulletin of the American Meteorologi-*
653 *cal Society*, 1–53. Retrieved from [http://journals.ametsoc.org/bams/](http://journals.ametsoc.org/bams/article-pdf/doi/10.1175/BAMS-D-20-0031.1/5018772/bamsd200031.pdf)
654 [article-pdf/doi/10.1175/BAMS-D-20-0031.1/5018772/bamsd200031.pdf](http://journals.ametsoc.org/bams/article-pdf/doi/10.1175/BAMS-D-20-0031.1/5018772/bamsd200031.pdf)
655 doi: 10.1175/BAMS-D-20-0031.1
- 656 Bykov, K., Höhne, M. M. C., Müller, K.-R., Nakajima, S., & Kloft, M. (2020, jun).
657 How Much Can I Trust You? – Quantifying Uncertainties in Explaining Neural
658 Networks. *arXiv*. Retrieved from <http://arxiv.org/abs/2006.09000>
- 659 Chemke, R., Zanna, L., & Polvani, L. M. (2020). Identifying a human signal in the
660 North Atlantic warming hole. *Nature Communications*, 11(1). doi: 10.1038/
661 s41467-020-15285-x
- 662 Compo, G. P., Whitaker, J. S., Sardeshmukh, P. D., Matsui, N., Allan, R. J.,

- 663 Yin, X., ... Worley, S. J. (2011, jan). *The Twentieth Century Reanalysis*
664 *Project* (Vol. 137) (No. 654). John Wiley and Sons Ltd. Retrieved from
665 <https://rmets.onlinelibrary.wiley.com/doi/full/10.1002/qj.776> doi:
666 10.1002/qj.776
- 667 Dagan, G., Stier, P., & Watson-Parris, D. (2020, nov). Aerosol forcing masks
668 and delays the formation of the North-Atlantic warming hole by three
669 decades. *Geophysical Research Letters*, 47(22). Retrieved from [https://](https://agupubs.onlinelibrary.wiley.com/doi/full/10.1029/2020GL090778)
670 agupubs.onlinelibrary.wiley.com/doi/full/10.1029/2020GL090778 doi:
671 10.1029/2020gl090778
- 672 Deng, J., Dai, A., & Xu, H. (2020, jan). Nonlinear climate responses to increas-
673 ing CO2 and anthropogenic aerosols simulated by CESM1. *Journal of Climate*,
674 33(1), 281–301. Retrieved from www.ametsoc.org/PUBSReuseLicenses doi:
675 10.1175/JCLI-D-19-0195.1
- 676 Deser, C. (2020, nov). Certain uncertainty: The role of internal climate variabil-
677 ity in projections of regional climate change and risk management. *Earth's*
678 *Future*. Retrieved from [https://onlinelibrary.wiley.com/doi/10.1029/](https://onlinelibrary.wiley.com/doi/10.1029/2020EF001854)
679 [2020EF001854](https://onlinelibrary.wiley.com/doi/10.1029/2020EF001854) doi: 10.1029/2020EF001854
- 680 Deser, C., Lehner, F., Rodgers, K. B., Ault, T., Delworth, T. L., DiNezio, P. N.,
681 ... Ting, M. (2020, mar). Insights from Earth system model initial-condition
682 large ensembles and future prospects. *Nature Climate Change*, 1–10. Re-
683 trieved from <http://www.nature.com/articles/s41558-020-0731-2> doi:
684 10.1038/s41558-020-0731-2
- 685 Deser, C., Phillips, A., Bourdette, V., & Teng, H. (2012, feb). Uncertainty in climate
686 change projections: the role of internal variability. *Climate Dynamics*, 38(3-4),
687 527–546. Retrieved from [http://link.springer.com/10.1007/s00382-010-](http://link.springer.com/10.1007/s00382-010-0977-x)
688 [-0977-x](http://link.springer.com/10.1007/s00382-010-0977-x) doi: 10.1007/s00382-010-0977-x
- 689 Deser, C., Phillips, A. S., Simpson, I. R., Rosenbloom, N., Coleman, D., Lehner, F.,
690 ... Stevenson, S. (2020, sep). Isolating the Evolving Contributions of An-
691 thropogenic Aerosols and Greenhouse Gases: A New CESM1 Large Ensemble
692 Community Resource. *Journal of Climate*, 33(18), 7835–7858. Retrieved from
693 <https://doi.org/10.1175/JCLI-D-20-> doi: 10.1175/JCLI-D-20-
- 694 Deser, C., Terray, L., & Phillips, A. S. (2016). Forced and internal compo-
695 nents of winter air temperature trends over North America during the past

- 696 50 years: Mechanisms and implications. *Journal of Climate*, 29(6). doi:
 697 10.1175/JCLI-D-15-0304.1
- 698 Dittus, A. J., Hawkins, E., Wilcox, L. J., Sutton, R. T., Smith, C. J., Andrews,
 699 M. B., & Forster, P. M. (2020, jul). Sensitivity of Historical Climate
 700 Simulations to Uncertain Aerosol Forcing. *Geophysical Research Letters*,
 701 47(13). Retrieved from [https://onlinelibrary.wiley.com/doi/10.1029/](https://onlinelibrary.wiley.com/doi/10.1029/2019GL085806)
 702 2019GL085806 doi: 10.1029/2019GL085806
- 703 Ebert-Uphoff, I., Samarasinghe, S., & Barnes, E. (2019). Thoughtfully Using Artificial
 704 Intelligence in Earth Science. *Eos*, 100. doi: 10.1029/2019eo135235
- 705 Fabi, K., & Schneider, J. (2020, aug). On Feature Relevance Uncertainty: A Monte
 706 Carlo Dropout Sampling Approach. *arXiv*. Retrieved from [http://arxiv](http://arxiv.org/abs/2008.01468)
 707 [.org/abs/2008.01468](http://dx.doi.org/10.5281/zenodo.3970396)<http://dx.doi.org/10.5281/zenodo.3970396> doi: 10
 708 .5281/zenodo.3970396
- 709 Flynn, C. M., & Mauritsen, T. (2020). On the climate sensitivity and historical
 710 warming evolution in recent coupled model ensembles. *Atmospheric Chemistry*
 711 *and Physics*, 20(13). doi: 10.5194/acp-20-7829-2020
- 712 Friedman, J. H. (2012, jul). Fast sparse regression and classification. *International*
 713 *Journal of Forecasting*, 28(3), 722–738. doi: 10.1016/j.ijforecast.2012.05.001
- 714 Gagne, D. J., Haupt, S. E., Nychka, D. W., & Thompson, G. (2019, aug). *In-*
 715 *terpretable deep learning for spatial analysis of severe hailstorms* (Vol. 147)
 716 (No. 8). American Meteorological Society. doi: 10.1175/MWR-D-18-0316.1
- 717 Giese, B. S., Seidel, H. F., Compo, G. P., & Sardeshmukh, P. D. (2016, sep).
 718 An ensemble of ocean reanalyses for 1815-2013 with sparse observational
 719 input. *Journal of Geophysical Research: Oceans*, 121(9), 6891–6910.
 720 Retrieved from <http://doi.wiley.com/10.1002/2016JC012079> doi:
 721 10.1002/2016JC012079
- 722 Goodfellow, I., Bengio, Y., & Courville, A. (2016). *Deep Learning*.
- 723 Harris, C. R., Jarrod Millman, K., van der Walt, S. J., Gommers, R., Virtanen, P.,
 724 Cournapeau, D., ... Oliphant, T. E. (2020, sep). Array programming with
 725 NumPy. *Nature*, 585(7825), 357. Retrieved from [https://doi.org/10.1038/](https://doi.org/10.1038/s41586-020-2649-2)
 726 [s41586-020-2649-2](https://doi.org/10.1038/s41586-020-2649-2) doi: 10.1038/s41586-020-2649-2
- 727 Haustein, K., Otto, F. E., Venema, V., Jacobs, P., Cowtan, K., Hausfather, Z.,
 728 ... Schurer, A. P. (2019). A limited role for unforced internal vari-

- 729 ability in twentieth-century warming. *Journal of Climate*, 32(16). doi:
730 10.1175/JCLI-D-18-0555.1
- 731 Hawkins, E., Ortega, P., Suckling, E., Schurer, A., Hegerl, G., Jones, P., ... Van
732 Oldenborgh, G. J. (2017, sep). Estimating changes in global temperature
733 since the preindustrial period. *Bulletin of the American Meteorological So-*
734 *ciety*, 98(9), 1841–1856. Retrieved from [http://journals.ametsoc.org/
735 bams/article-pdf/98/9/1841/3747963/bams-d-16-0007{_}_}1.pdf](http://journals.ametsoc.org/bams/article-pdf/98/9/1841/3747963/bams-d-16-0007{_}_}1.pdf) doi:
736 10.1175/BAMS-D-16-0007.1
- 737 Hawkins, E., & Sutton, R. (2009, aug). The Potential to Narrow Uncertainty in
738 Regional Climate Predictions. *Bulletin of the American Meteorological Society*,
739 90(8), 1095–1107. doi: 10.1175/2009BAMS2607.1
- 740 Hawkins, E., & Sutton, R. (2016, jun). Connecting climate model projections
741 of global temperature change with the real world. *Bulletin of the Amer-*
742 *ican Meteorological Society*, 97(6), 963–980. Retrieved from [https://
743 journals.ametsoc.org/view/journals/bams/97/6/bams-d-14-00154.1.xml](https://journals.ametsoc.org/view/journals/bams/97/6/bams-d-14-00154.1.xml)
744 doi: 10.1175/BAMS-D-14-00154.1
- 745 Hegerl, G. C., Von Storch, H., Hasselmann, K., Santer, B. D., Cubasch, U., &
746 Jones, P. D. (1996). Detecting greenhouse-gas-induced climate change
747 with an optimal fingerprint method. *Journal of Climate*, 9(10). doi:
748 10.1175/1520-0442(1996)009<2281:DG GICC>2.0.CO;2
- 749 Hersbach, H., Bell, B., Berrisford, P., Hirahara, S., Horányi, A., Muñoz-Sabater,
750 J., ... Thépaut, J.-N. (2020, may). The ERA5 Global Reanalysis.
751 *Quarterly Journal of the Royal Meteorological Society*. Retrieved from
752 <https://onlinelibrary.wiley.com/doi/abs/10.1002/qj.3803> doi:
753 10.1002/qj.3803
- 754 Hunter, J. D. (2007, may). Matplotlib: A 2D graphics environment. *Computing in*
755 *Science and Engineering*, 9(3), 99–104. doi: 10.1109/MCSE.2007.55
- 756 Hurrell, J. W., Holland, M. M., Gent, P. R., Ghan, S., Kay, J. E., Kushner, P. J.,
757 ... Marshall, S. (2013). The community earth system model: A framework for
758 collaborative research. *Bulletin of the American Meteorological Society*, 94(9).
759 doi: 10.1175/BAMS-D-12-00121.1
- 760 Kadow, C., Hall, D. M., & Ulbrich, U. (2020, jun). Artificial intelligence reconstructs
761 missing climate information. *Nature Geoscience*, 1–6. doi: 10.1038/s41561-020

-0582-5

- 762
- 763 Kay, J. E., Deser, C., Phillips, A., Mai, A., Hannay, C., Strand, G., . . . Verten-
- 764 stein, M. (2015, aug). The Community Earth System Model (CESM)
- 765 Large Ensemble Project: A Community Resource for Studying Climate
- 766 Change in the Presence of Internal Climate Variability. *Bulletin of the*
- 767 *American Meteorological Society*, 96(8), 1333–1349. Retrieved from
- 768 <http://journals.ametsoc.org/doi/10.1175/BAMS-D-13-00255.1> doi:
- 769 10.1175/BAMS-D-13-00255.1
- 770 Keil, P., Mauritsen, T., Jungclaus, J., Hedemann, C., Olonscheck, D., & Ghosh, R.
- 771 (2020). Multiple drivers of the North Atlantic warming hole. *Nature Climate*
- 772 *Change*, 10(7). doi: 10.1038/s41558-020-0819-8
- 773 Knutti, R., Furrer, R., Tebaldi, C., Cermak, J., & Meehl, G. A. (2010). Challenges
- 774 in combining projections from multiple climate models. *Journal of Climate*,
- 775 23(10). doi: 10.1175/2009JCLI3361.1
- 776 Knutti, R., & Sedlacek, J. (2013, apr). Robustness and uncertainties in the new
- 777 CMIP5 climate model projections. *Nature Clim. Change*, 3(4), 369–373. doi:
- 778 10.1038/nclimate1716
- 779 Lagerquist, R., McGovern, A., Homeyer, C. R., Gagne, D. J., & Smith, T. (2020,
- 780 jul). Deep learning on three-dimensional multiscale data for next-hour
- 781 tornado prediction. *Monthly Weather Review*, 148(7), 2837–2861. doi:
- 782 10.1175/MWR-D-19-0372.1
- 783 Lecun, Y., Bengio, Y., & Hinton, G. (2015, may). *Deep learning* (Vol. 521) (No.
- 784 7553). Nature Publishing Group. Retrieved from [https://www.nature.com/](https://www.nature.com/articles/nature14539)
- 785 [articles/nature14539](https://www.nature.com/articles/nature14539) doi: 10.1038/nature14539
- 786 Lehner, F., Deser, C., Maher, N., Marotzke, J., Fischer, E., Brunner, L., . . .
- 787 Hawkins, E. (2020). Partitioning climate projection uncertainty with mul-
- 788 tiple Large Ensembles and CMIP5/6. *Earth System Dynamics Discussions*,
- 789 1–28. doi: 10.5194/esd-2019-93
- 790 Luysaert, S., Jammet, M., Stoy, P. C., Estel, S., Pongratz, J., Ceschia, E., . . .
- 791 Dolman, A. J. (2014, apr). Land management and land-cover change have
- 792 impacts of similar magnitude on surface temperature. *Nature Climate Change*,
- 793 4(5), 389–393. Retrieved from www.nature.com/natureclimatechange doi:
- 794 10.1038/nclimate2196

- 795 Maher, N., Gupta, A. S., & England, M. H. (2014). *Drivers of decadal hiatus*
796 *periods in the 20th and 21st centuries* (Vol. 41) (No. 16). doi: 10.1002/
797 2014GL060527
- 798 Maher, N., Lehner, F., & Marotzke, J. (2020, may). Quantifying the role of internal
799 variability in the temperature we expect to observe in the coming decades.
800 *Environmental Research Letters*, 15(5), 054014. Retrieved from [https://](https://doi.org/10.1088/1748-9326/ab7d02)
801 doi.org/10.1088/1748-9326/ab7d02 doi: 10.1088/1748-9326/ab7d02
- 802 Maher, N., Milinski, S., Suarez-Gutierrez, L., Botzet, M., Dobrynin, M., Kornblueh,
803 L., ... Marotzke, J. (2019, jul). The Max Planck Institute Grand Ensemble:
804 Enabling the Exploration of Climate System Variability. *Journal of Advances*
805 *in Modeling Earth Systems*, 11(7), 2050–2069. Retrieved from [https://](https://agupubs.onlinelibrary.wiley.com/doi/full/10.1029/2019MS001639)
806 agupubs.onlinelibrary.wiley.com/doi/full/10.1029/2019MS001639 doi:
807 10.1029/2019MS001639
- 808 Mankin, J. S., Lehner, F., Coats, S., & McKinnon, K. A. (2020, oct). The Value
809 of Initial Condition Large Ensembles to Robust Adaptation Decision-Making.
810 *Earth's Future*, 8(10). Retrieved from [https://onlinelibrary.wiley.com/](https://onlinelibrary.wiley.com/doi/10.1029/2020EF001610)
811 [doi/10.1029/2020EF001610](https://onlinelibrary.wiley.com/doi/10.1029/2020EF001610) doi: 10.1029/2020EF001610
- 812 Mann, H. B. (1945). Nonparametric Tests Against Trend. *Econometrica*. doi: 10
813 .2307/1907187
- 814 Mansfield, L. A., Nowack, P. J., Kasoar, M., Everitt, R. G., Collins, W. J., & Voul-
815 garakis, A. (2020). Predicting global patterns of long-term climate change from
816 short-term simulations using machine learning. *npj Climate and Atmospheric*
817 *Science*. Retrieved from <https://doi.org/10.1038/s41612-020-00148-5>
818 doi: 10.1038/s41612-020-00148-5
- 819 Marvel, K., Cook, B. I., Bonfils, C. J., Durack, P. J., Smerdon, J. E., & Williams,
820 A. P. (2019). Twentieth-century hydroclimate changes consistent with human
821 influence. *Nature*, 569(7754). doi: 10.1038/s41586-019-1149-8
- 822 McGovern, A., Lagerquist, R., Gagne, D. J., Jergensen, G. E., Elmore, K. L., Home-
823 yer, C. R., & Smith, T. (2019, nov). Making the black box more transparent:
824 Understanding the physical implications of machine learning. *Bulletin of*
825 *the American Meteorological Society*, 100(11), 2175–2199. Retrieved from
826 [http://journals.ametsoc.org/bams/article-pdf/100/11/2175/4876688/](http://journals.ametsoc.org/bams/article-pdf/100/11/2175/4876688/bams-d-18-0195-v1.pdf)
827 [bams-d-18-0195-v1.pdf](http://journals.ametsoc.org/bams/article-pdf/100/11/2175/4876688/bams-d-18-0195-v1.pdf) doi: 10.1175/BAMS-D-18-0195.1

- 828 McKinnon, K. A., & Deser, C. (2018). Internal variability and regional climate
 829 trends in an observational large ensemble. *Journal of Climate*, *31*(17). doi: 10
 830 .1175/JCLI-D-17-0901.1
- 831 Medhaug, I., Stolpe, M. B., Fischer, E. M., & Knutti, R. (2017). *Reconciling contro-*
 832 *versies about the 'global warming hiatus'* (Vol. 545) (No. 7652). doi: 10.1038/
 833 nature22315
- 834 Meehl, G. A., Hu, A., Castruccio, F., England, M. H., Bates, S. C., Danabasoglu,
 835 G., ... Rosenbloom, N. (2020). Atlantic and Pacific tropics connected
 836 by mutually interactive decadal-timescale processes. *Nature Geoscience*.
 837 Retrieved from <https://doi.org/10.1038/s41561-020-00669-x> doi:
 838 10.1038/s41561-020-00669-x
- 839 Meehl, G. A., Senior, C. A., Eyring, V., Flato, G., Lamarque, J. F., Stouffer, R. J.,
 840 ... Schlund, M. (2020). *Context for interpreting equilibrium climate sensitivity*
 841 *and transient climate response from the CMIP6 Earth system models* (Vol. 6)
 842 (No. 26). doi: 10.1126/sciadv.aba1981
- 843 Menary, M. B., Robson, J., Allan, R. P., Booth, B. B., Cassou, C., Gastineau,
 844 G., ... Zhang, R. (2020). Aerosol-Forced AMOC Changes in CMIP6
 845 Historical Simulations. *Geophysical Research Letters*, *47*(14). doi:
 846 10.1029/2020GL088166
- 847 Milinski, S., Maher, N., & Olonscheck, D. (2020, oct). How large does a large en-
 848 semble need to be? *Earth System Dynamics*, *11*(4), 885–901. Retrieved from
 849 <https://esd.copernicus.org/articles/11/885/2020/> doi: 10.5194/esd-11
 850 -885-2020
- 851 Mitchell, D. M., Eunice Lo, Y. T., Seviour, W. J., Haimberger, L., & Polvani, L. M.
 852 (2020, oct). The vertical profile of recent tropical temperature trends: Persis-
 853 tent model biases in the context of internal variability. *Environmental Research*
 854 *Letters*, *15*(10). doi: 10.1088/1748-9326/ab9af7
- 855 Montavon, G., Lapuschkin, S., Binder, A., Samek, W., & Müller, K. R. (2017, may).
 856 Explaining nonlinear classification decisions with deep Taylor decomposition.
 857 *Pattern Recognition*, *65*, 211–222. doi: 10.1016/j.patcog.2016.11.008
- 858 Montavon, G., Samek, W., & Müller, K. R. (2018, feb). *Methods for interpreting and*
 859 *understanding deep neural networks* (Vol. 73). Elsevier Inc. doi: 10.1016/j.dsp
 860 .2017.10.011

- 861 Neale, R. B., Gettelman, A., Park, S., Chen, C.-c., Lauritzen, P. H., Williamson,
862 D. L., . . . Taylor, M. a. (2012). Description of the NCAR Community Atmo-
863 sphere Model (CAM 5.0). NCAR Technical Notes. *Ncar/Tn-464+Str*.
- 864 Oudar, T., Kushner, P. J., Fyfe, J. C., & Sigmond, M. (2018, sep). No Impact of
865 Anthropogenic Aerosols on Early 21st Century Global Temperature Trends
866 in a Large Initial-Condition Ensemble. *Geophysical Research Letters*, *45*(17),
867 9245–9252. Retrieved from <http://doi.wiley.com/10.1029/2018GL078841>
868 doi: 10.1029/2018GL078841
- 869 Peace, A. H., Carslaw, K. S., Lee, L. A., Regayre, L. A., Booth, B. B., Johnson,
870 J. S., & Bernie, D. (2020). Effect of aerosol radiative forcing uncertainty on
871 projected exceedance year of a 1.5 °c global temperature rise. *Environmental*
872 *Research Letters*, *15*(9). doi: 10.1088/1748-9326/aba20c
- 873 Peters, G. P., & Hausfather, Z. (2020). Emissions - the 'business as usual' story is
874 misleading. *Nature*, *577*.
- 875 Polvani, L. M., Waugh, D. W., Correa, G. J., & Son, S. W. (2011, feb). Strato-
876 spheric ozone depletion: The main driver of twentieth-century atmospheric
877 circulation changes in the Southern Hemisphere. *Journal of Climate*, *24*(3),
878 795–812. Retrieved from [http://journals.ametsoc.org/jcli/article-pdf/
879 24/3/795/3979461/2010jcli3772_{_}1.pdf](http://journals.ametsoc.org/jcli/article-pdf/24/3/795/3979461/2010jcli3772_{_}1.pdf) doi: 10.1175/2010JCLI3772.1
- 880 Qin, M., Dai, A., & Hua, W. (2020, oct). Quantifying contributions of internal
881 variability and external forcing to Atlantic multidecadal variability since
882 1870. *Geophysical Research Letters*, *47*(22). Retrieved from [https://
883 agupubs.onlinelibrary.wiley.com/doi/full/10.1029/2020GL089504](https://agupubs.onlinelibrary.wiley.com/doi/full/10.1029/2020GL089504)
884 doi: 10.1029/2020gl089504
- 885 Rasp, S., Dueben, P. D., Scher, S., Weyn, J. A., Mouatadid, S., & Thuerey, N.
886 (2020, feb). *Weatherbench: A benchmark dataset for data-driven weather fore-
887 casting* (Vol. 12) (No. 11). American Geophysical Union (AGU). Retrieved
888 from [https://agupubs.onlinelibrary.wiley.com/doi/full/10.1029/
889 2020MS002203](https://agupubs.onlinelibrary.wiley.com/doi/full/10.1029/2020MS002203) doi: 10.1029/2020ms002203
- 890 Rasp, S., Pritchard, M. S., & Gentine, P. (2018, sep). Deep learning to represent
891 subgrid processes in climate models. *Proceedings of the National Academy*
892 *of Sciences of the United States of America*, *115*(39), 9684–9689. Retrieved
893 from <https://gitlab.com/mspritch/spcam3.0-neural-net/tree/nn> doi:

- 894 10.1073/pnas.1810286115
- 895 Rasu, E., Bernstein, R., Huntingford, C., Jeffers, E. S., Bonsall, M. B., Christensen,
896 H. M., ... Yang, H. (2019). Machine learning and artificial intelligence
897 to aid climate change research and preparedness. *Environ. Res. Lett*, *14*,
898 124007. Retrieved from <https://doi.org/10.1088/1748-9326/ab4e55> doi:
899 10.1088/1748-9326/ab4e55
- 900 Ruder, S. (2016, sep). An overview of gradient descent optimization algorithms.
901 *arXiv*. Retrieved from <http://arxiv.org/abs/1609.04747>
- 902 Samek, W., Binder, A., Montavon, G., Lapuschkin, S., & Müller, K. R. (2017).
903 Evaluating the visualization of what a deep neural network has learned.
904 *IEEE Transactions on Neural Networks and Learning Systems*, *28*(11). doi:
905 10.1109/TNNLS.2016.2599820
- 906 Samek, W., Montavon, G., Lapuschkin, S., Anders, C. J., & Müller, K.-R. (2020,
907 mar). Toward Interpretable Machine Learning: Transparent Deep Neural
908 Networks and Beyond. *arXiv*. Retrieved from [http://arxiv.org/abs/](http://arxiv.org/abs/2003.07631)
909 [2003.07631](http://arxiv.org/abs/2003.07631)
- 910 Santer, B. D., Fyfe, J. C., Solomon, S., Painter, J. F., Bonfils, C., Pallotta, G., &
911 Zelinka, M. D. (2019, oct). Quantifying stochastic uncertainty in detection
912 time of human-caused climate signals. *Proceedings of the National Academy*
913 *of Sciences of the United States of America*, *116*(40), 19821–19827. Retrieved
914 from www.pnas.org/cgi/doi/10.1073/pnas.1922907117 doi:
915 10.1073/pnas.1904586116
- 916 Schneider, T., & Held, I. M. (2001). Discriminants of twentieth-century changes
917 in earth surface temperatures. *Journal of Climate*, *14*(3). doi: 10.1175/1520
918 -0442(2001)014<0249:LDOTCC>2.0.CO;2
- 919 Sherwood, S. C., Webb, M. J., Annan, J. D., Armour, K. C., Forster, P. M., Har-
920 greaves, J. C., ... Zelinka, M. D. (2020, dec). An Assessment of Earth's
921 Climate Sensitivity Using Multiple Lines of Evidence. *Reviews of Geophysics*,
922 *58*(4). Retrieved from [https://agupubs.onlinelibrary.wiley.com/doi/](https://agupubs.onlinelibrary.wiley.com/doi/full/10.1029/2019RG000678)
923 [full/10.1029/2019RG000678](https://agupubs.onlinelibrary.wiley.com/doi/full/10.1029/2019RG000678) doi: 10.1029/2019rg000678
- 924 Sippel, S., Meinshausen, N., Fischer, E. M., Székely, E., & Knutti, R. (2020, jan).
925 *Climate change now detectable from any single day of weather at global scale*
926 (Vol. 10) (No. 1). Nature Research. doi: 10.1038/s41558-019-0666-7

- 927 Sippel, S., Meinshausen, N., Merrifield, A., Lehner, F., Pendergrass, A. G., Fischer,
 928 E., & Knutti, R. (2019). Uncovering the forced climate response from a single
 929 ensemble member using statistical learning. *Journal of Climate*, *32*(17). doi:
 930 10.1175/JCLI-D-18-0882.1
- 931 Slivinski, L. C., Compo, G. P., Sardeshmukh, P. D., Whitaker, J. S., McColl, C.,
 932 Allan, R. J., ... Wyszyński, P. (2020, dec). An evaluation of the performance
 933 of the 20th Century Reanalysis version 3. *Journal of Climate*, *-1*(aop), 1–64.
 934 Retrieved from [https://journals.ametsoc.org/view/journals/clim/aop/
 935 JCLI-D-20-0505.1/JCLI-D-20-0505.1.xml](https://journals.ametsoc.org/view/journals/clim/aop/JCLI-D-20-0505.1/JCLI-D-20-0505.1.xml) doi: 10.1175/JCLI-D-20-0505.1
- 936 Slivinski, L. C., Compo, G. P., Whitaker, J. S., Sardeshmukh, P. D., Giese, B. S.,
 937 McColl, C., ... Wyszyński, P. (2019, oct). Towards a more reliable historical
 938 reanalysis: Improvements for version 3 of the Twentieth Century Reanalysis
 939 system. *Quarterly Journal of the Royal Meteorological Society*, *145*(724),
 940 2876–2908. Retrieved from [https://onlinelibrary.wiley.com/doi/abs/
 941 10.1002/qj.3598](https://onlinelibrary.wiley.com/doi/abs/10.1002/qj.3598) doi: 10.1002/qj.3598
- 942 Smith, C., Kramer, R., Myhre, G., Alterskjr, K., Collins, W., Sima, A., ... M.
 943 Forster, P. (2020). Effective radiative forcing and adjustments in CMIP6
 944 models. *Atmospheric Chemistry and Physics*, *20*(16). doi: 10.5194/
 945 acp-20-9591-2020
- 946 Smith, D. M., Booth, B. B., Dunstone, N. J., Eade, R., Hermanson, L., Jones, G. S.,
 947 ... Thompson, V. (2016). Role of volcanic and anthropogenic aerosols in the
 948 recent global surface warming slowdown. *Nature Climate Change*, *6*(10). doi:
 949 10.1038/nclimate3058
- 950 Stocker, T. F., Qin, D., Plattner, G. K., Tignor, M. M., Allen, S. K., Boschung,
 951 J., ... Midgley, P. M. (2013). *Climate change 2013 the physical sci-*
 952 *ence basis: Working Group I contribution to the fifth assessment report*
 953 *of the intergovernmental panel on climate change* (Vol. 9781107057). doi:
 954 10.1017/CBO9781107415324
- 955 Stott, P. A., Mitchell, J. F., Allen, M. R., Delworth, T. L., Gregory, J. M., Meehl,
 956 G. A., & Santer, B. D. (2006). Observational constraints on past attributable
 957 warming and predictions of future global warming. *Journal of Climate*, *19*(13).
 958 doi: 10.1175/JCLI3802.1
- 959 Thorsen, T. J., Winker, D. M., & Ferrare, R. A. (2020, oct). Uncertainty in obser-

- 960 vational estimates of the aerosol direct radiative effect and forcing. *Journal of*
961 *Climate*, 34(1), 1–63. Retrieved from [https://journals.ametsoc.org/view/](https://journals.ametsoc.org/view/journals/clim/34/1/jcliD191009.xml)
962 [journals/clim/34/1/jcliD191009.xml](https://journals.ametsoc.org/view/journals/clim/34/1/jcliD191009.xml) doi: 10.1175/jcli-d-19-1009.1
- 963 Thyng, K., Greene, C., Hetland, R., Zimmerle, H., & DiMarco, S. (2016, sep). True
964 Colors of Oceanography: Guidelines for Effective and Accurate Colormap
965 Selection. *Oceanography*, 29(3), 9–13. Retrieved from [https://tos.org/](https://tos.org/oceanography/article/true-colors-of-oceanography-guidelines-for-effective-and-accurate-colormap)
966 [oceanography/article/true-colors-of-oceanography-guidelines-for](https://tos.org/oceanography/article/true-colors-of-oceanography-guidelines-for-effective-and-accurate-colormap)
967 [-effective-and-accurate-colormap](https://tos.org/oceanography/article/true-colors-of-oceanography-guidelines-for-effective-and-accurate-colormap) doi: 10.5670/oceanog.2016.66
- 968 Toms, B. A., Barnes, E. A., & Ebert-Uphoff, I. (2020, sep). Physically Interpretable
969 Neural Networks for the Geosciences: Applications to Earth System Vari-
970 ability. *Journal of Advances in Modeling Earth Systems*, 12(9). Retrieved
971 from <https://onlinelibrary.wiley.com/doi/10.1029/2019MS002002> doi:
972 10.1029/2019MS002002
- 973 Virtanen, P., Gommers, R., Oliphant, T. E., Haberland, M., Reddy, T., Courn-
974 peau, D., ... Vázquez-Baeza, Y. (2020). SciPy 1.0: fundamental algo-
975 rithms for scientific computing in Python. *Nature Methods*, 17(3). doi:
976 10.1038/s41592-019-0686-2
- 977 Vuuren, D. P., Edmonds, J., Kainuma, M., Riahi, K., Thomson, A., Hibbard,
978 K., ... Rose, S. K. (2011, aug). The representative concentration path-
979 ways: an overview. *Climatic Change*, 109(1-2), 5–31. Retrieved from
980 <http://link.springer.com/10.1007/s10584-011-0148-z> doi: 10.1007/
981 s10584-011-0148-z
- 982 Wang, H., Xie, S., Zheng, X., Kosaka, Y., Xu, Y., & Geng, Y. (2020, oct). Dy-
983 namics of Southern Hemisphere Atmospheric Circulation Response to Anthro-
984 pogenic Aerosol Forcing. *Geophysical Research Letters*, 47(19). Retrieved
985 from <https://onlinelibrary.wiley.com/doi/10.1029/2020GL089919> doi:
986 10.1029/2020GL089919
- 987 Watson-Parris, D. (2020, aug). Machine learning for weather and climate are worlds
988 apart. *arXiv*. Retrieved from <http://arxiv.org/abs/2008.10679>
- 989 Weyn, J. A., Durran, D. R., & Caruana, R. (2020, sep). Improving Data-Driven
990 Global Weather Prediction Using Deep Convolutional Neural Networks
991 on a Cubed Sphere. *Journal of Advances in Modeling Earth Systems*,
992 12(9). Retrieved from <https://onlinelibrary.wiley.com/doi/10.1029/>

- 993 2020MS002109 doi: 10.1029/2020MS002109
- 994 Wills, R., Battisti, D. S., Armour, K. C., Schneider, T., & Deser, C. (2020, sep).
995 Pattern Recognition Methods to Separate Forced Responses from Internal
996 Variability in Climate Model Ensembles and Observations. *Journal of Climate*,
997 *33*(20), 8693–8719. Retrieved from <https://doi.org/10.1175/JCLI-D-19-19-0855.1>
998 doi: 10.1175/JCLI-D-19-0855.1
- 999 Wills, R., Sippel, S., & Barnes, E. A. (2020). Separating forced and unforced
1000 components of climate change: The utility of pattern recognition methods
1001 in Large Ensembles and observations. *US CLIVAR Variations*, *18*(2). doi:
1002 10.5065/0DSY-WH17
- 1003 Yoshioka, M., Regayre, L. A., Pringle, K. J., Johnson, J. S., Mann, G. W., Par-
1004 tridge, D. G., ... Carslaw, K. S. (2019). Ensembles of Global Climate Model
1005 Variants Designed for the Quantification and Constraint of Uncertainty in
1006 Aerosols and Their Radiative Forcing. *Journal of Advances in Modeling Earth
1007 Systems*, *11*(11). doi: 10.1029/2019MS001628
- 1008 Zadeh, L. A. (1965, jun). Fuzzy sets. *Information and Control*, *8*(3), 338–353. doi:
1009 10.1016/S0019-9958(65)90241-X
- 1010 Zanna, L., & Bolton, T. (2020, sep). Data-Driven Equation Discovery of Ocean
1011 Mesoscale Closures. *Geophysical Research Letters*, *47*(17). Retrieved from
1012 <https://onlinelibrary.wiley.com/doi/10.1029/2020GL088376> doi:
1013 10.1029/2020GL088376
- 1014 Zelinka, M. D., Andrews, T., Forster, P. M., & Taylor, K. E. (2014, jun). Quan-
1015 tifying components of aerosol-cloud-radiation interactions in climate models.
1016 *Journal of Geophysical Research: Atmospheres*, *119*(12), 7599–7615. Retrieved
1017 from [https://agupubs.onlinelibrary.wiley.com/doi/full/10.1002/](https://agupubs.onlinelibrary.wiley.com/doi/full/10.1002/2014JD021710)
1018 [2014JD021710](https://agupubs.onlinelibrary.wiley.com/doi/full/10.1002/2014JD021710) doi: 10.1002/2014JD021710